Predicting Metal-Support Interactions in Oxide-Supported Single-Atom Catalysts

by

Kaiyang Tan

B.S. Material Chemistry, University of Science and Technology of China, 2017

Submitted to the Graduate Faculty of

Swanson School of Engineering in partial fulfillment

of the requirements for the degree of

Master of Science

University of Pittsburgh

2019

UNIVERSITY OF PITTSBURGH

SWANSON SCHOOL OF ENGINEERING

This thesis was presented

by

Kaiyang Tan

It was defended on

July 10, 2019

and approved by

Goetz Veser, Ph.D., Professor
Department of Chemical and Petroleum Engineering

J Karl Johnson, Ph.D., W.K. Whiteford Professor
Department of Chemical and Petroleum Engineering

Thesis Advisor: Giannis Mpourmpakis, Assistant Professor
Department of Chemical and Petroleum Engineering

Predicting Metal-Support Interactions in Oxide-Supported Single-Atom Catalysts

Kaiyang Tan, M.S.

University of Pittsburgh, 2019

Single-Atom Catalysts (SACs), containing under-coordinated single metal atoms bound on the surface of supports, have recently emerged as promising heterogeneous catalysts due to their intrinsic catalytic properties and efficient utilization (high dispersion) of noble metal atoms. Strong Metal-Support Interactions (MSIs) present in these catalysts can dictate the physicochemical properties, activity, and stability of SACs, which are significantly different from the conventional supported nanoscale metal catalysts. Although SACs exhibit unique catalytic behavior, their stability under catalytic operation is questioned due to the tendency of metals to sinter (aggregation). An optimal MSI can avoid metal aggregation and tune the stability and catalytic activity of SACs. Herein, we investigate MSIs of a series of transition metal atoms (Au, Cu, Ag, Pt, Pd, Ni, Rh, and Ir) supported on low-index surface facets of three oxides (γ-Al_2O_3, MgO, and $MgAl_2O_4$) that are commonly used as supports in catalysis. By investigating the adsorption of the metals at different binding sites across the oxide surfaces, we identify the best descriptors of MSI to be the gas-phase metal-oxygen binding energy and the oxide support's band gap. Moreover, utilizing the results of Density-Functional Theory (DFT) calculations and genetic programming, we develop a predictive model for the strength of MSI (which we quantify as adsorption energy) using simple properties of the SAC and the support. Finally, we introduce some guidelines to hypothesize the synthetic accessibility of a series of SACs based on thermodynamic arguments. Our computational work can guide experimentation by identifying combinations of metals and oxides that can potentially lead to highly stable (and catalytically durable) SACs.

Table of Contents

List of Tables

List of Figures

Preface

First, I would like to thank my thesis advisor, Dr. Giannis Mpourmpakis. His strict and warm-hearted guidance educated me a lot. In the past two years I enjoyed a busy but beneficial life in his lab, where I learnt new tools and methods every day. Second, I would like to thank Dr. Mudit. He helped me a lot in literature search and paper writing. I am also grateful to the students in the lab. They are all experienced researchers and never refused to help me when I was confused. I also want to thank the University of Pittsburgh and the Department of Chemical Engineering for providing me valuable research opportunities. Last but not least, I would like to thank my parents because of their physical and mental support. I hope my research in this thesis can help other scientists in the future.

1.0 Introduction

Single-Atom Catalysts (SACs) are a new frontier to increase the utilization of metal atoms in catalysis: the catalytic metal is dispersed on the support atomically, making all metal atoms accessible for catalysis[1-6]. Due to the under-coordination of the metal, quantum size effects, and strong Metal-Support Interactions (MSIs)[3-4], SACs also exhibit high catalytic activity and selectivity in a wide range of chemical transformations[3, 5].

Because of the strong cohesive energy and high surface energy of single metal atoms, the active metals of SACs have the thermodynamic tendency to sinter, which raises obvious problems regarding the stability of SACs under realistic catalytic conditions[7-9]. Sintering of SACs reduces their catalytic activity[10-12] by reducing the surface area and increasing the average coordination of the metal atoms[13]. Strong MSIs can mitigate sintering by anchoring metals to the support, stabilizing the SACs and preserving their high surface area. For instance, in the case of Pt_1/FeO_x, despite the high surface free energies of single Pt atoms, the Pt atoms are stabilized on the support via the formation of Pt-O-Fe metal-support bonds[14]. It has also been shown that the MSIs can dictate the performance of SACs, making it feasible to tune their catalytic activity, selectivity, and stability during catalytic operation[15-17].

Recent years a number of research efforts have focused on characterizing MSIs through both experiment (such as utilizing aberration-corrected environmental TEM chambers to dynamically study MSIs[18]) and computation (using Density-Functional Theory (DFT) and statistical learning to generate predictive models[19]). Despite this attention, a fundamental understanding of the primary interactions in SACs is still lacking. To understand MSIs, one needs to identify simple

descriptors for the strength of MSI (quantified in this work as the metal adsorption energy of SACs), ideally based on fundamental physical properties of the supported metals and the supports. Several outstanding works have demonstrated linear relationships between metal adsorption energy and metal-support pair properties (for SACs or other supported metal nanoparticles) such as surface energy of the metal, metal oxidation enthalpy[20], heat of metal oxide formation[21], and support reducibility[22]. These findings suggest that MSIs are influenced by the properties of both the metal and the support. Recently, O'Connor et al[19] applied statistical leaning methods to build predictive models of MISs by including various metal-support properties and investigated a large set of descriptors and predictive models for adsorption energy.

1.1 Single Atom Catalyst

Catalysts play an important role in various chemical and biological transformations through controlling the rates of both desired and undesired reactions[1, 23-24]. Among different homogeneous and heterogeneous catalysts, due to their ability to change oxidation states and form complexes, Transition Metal Nanoparticles (TMNPs) play a dominant role in catalysis[2-3, 25]. Since catalysis occurs at the surface of TMNP-based catalysts, only the surface metal atoms can be utilized as active catalytic sites. As a result, the subsurface atoms of TMNPs are essentially wasted and introduce an extra economic cost to industrial processes[1-2]. In order to maximize the ratio of exposed metal atoms, an obvious solution is to make the TMNP as small as possible. Efforts to reduce TMNP size have led to the development of SACs.

Recently, a series of noble metal SACs were synthesized and characterized on a variety of supports[26-35]. For instance, Pd_1/MgO (100) synthesized by high frequency laser evaporation shows

a unique size effect: the Pd cluster size governs the reacting temperature and mechanism of the catalyzed cyclotrimerization of acetylene to benzene[36]. Pt_1/Graphene has been successfully synthesized by atomic layer deposition and exhibits a high activity for methanol oxidation with superior tolerance for CO. This catalyst has excellent performance due to low-coordination and the presence of unsaturated 5d orbitals of the single Pt atom[37]. Rh/ZnO nanowires have been fabricated via the facile adsorption method. When catalyzing the hydroformylation of olefins, these nanowires exhibit levels of activity orders of magnitude higher than typical heterogeneous catalysts[38]. A well-known SAC is Ir_1/FeO_x, whose water-gas shift activity is an order of magnitude higher than its TMNP [14]. Overall, SACs show great promise in catalyzing a variety of reactions[14, 27, 36], even though this new frontier in catalysis has yet to be commercially-exploited[1].

2.0 Methodology

DFT calculations were performed by using the CP2K[46] package. The Perdew-Burke-Ernzerhof (PBE) exchange-correlation functional[47] was used in combination with Grimme's D3 dispersion-correction method[48]. Dipole corrections[49] were also added to accurately investigate asymmetric slab systems. TZVP basis sets[50] were used for O; DZVP basis sets[50] were used for Al, Mg, Au, Cu, Ag, Pt, Pd, Ni, Rh, and Ir. Additionally, we use the pseudopotentials of Goedecker, Teter, and Hutter[51-53] with a kinetic energy cutoff 400 Ry. We use a 1×1×1 "supercell" for γ-Al_2O_3 and $MgAl_2O_4$ due to their already-large unit cell. We use a 2×2×2 supercell for the bulk optimization of MgO. Following optimization of the bulk, we cleave the supercells to construct slabs. We use a 2×1 slab with 2 layers of repeating supercell for γ-Al_2O_3, a 1×1 slab with 1 layer of repeating supercell for MgO, and a 2×1 slab with 1 layer of repeating supercell for $MgAl_2O_4$. The two bottom atomic layers remaining fixed in their cell positions. Systems were relaxed with a force-convergence criterion of 0.0004 E_h/bohr, and an SCF convergence criterion of 10^{-8} au. Metal adsorption energy is calculated by Equation 2-1, where E_{ads} is the metal atom adsorption energy, $E_{M\text{-}support}$ is the total energy of the metal-support system, $E_{support}$ is the energy of the support, and E_M is the gas phase energy of the single metal atom.

$$E_{ads} = E_{M\text{-}support} - E_{support} - E_M \quad (2\text{-}1)$$

The metal-oxygen binding energy of supported metal is calculated by CP2K program package[46] and all metals are considered as +2 oxidation state[54]. To calculate the metal-oxygen binding energy (E_{M-O}) accurately (listed in Table S3c), we calculate the energy of a gas phase metal binding with a single oxygen atom (E_{M+O}). We investigate several different spin-states (listed in Table S3c) and choose the spin-state minimizing the energy of the metal-oxygen complex in order to investigate the energies accurately. E_O is gas phase energy of an oxygen atom. The metal-oxygen binding energy is calculated by Equation 2-2.

$$E_{M-O} = E_{M+O} - E_M - E_O \tag{2-2}$$

All gas phase energies of atoms are calculated in a 10*10*10 $Å^3$ cube.

2.1 Density Functional Theory

To study the atomistic interactions of the many-body electronic structure by ab initio methods, we need to solve the Schrodinger's equation[39]. However, this is very expensive in computation since the wavefunction of many-body systems depends on the number of electrons of every individual particles. Density Functional Theory (DFT) is an approach to calculate the ground state properties of a many-electron system[40] in condensed matter physics and chemistry[41] using the functional of electron density. This approach provides a balance between the system size and computational cost during the calculation of electronic structure. Yet according to Hohenberg-

Kohn (H-K) theorem[42], the energies of interacting electrons remain unknown, which produces limitations to original DFT calculations. In Kohn-Sham (KS) DFT[43], the energies of interacting electrons are regarded as electrons moving into a static external potential by fictitious orbitals without interacting with other particles. The sum of densities of occupied orbitals represents the overall ground-state density of the system.

$$(r) = \sum |\varphi_i(r)|^2 \tag{2-3}$$

In equation 1-1, $\varphi_i(r)$ is Kohn-Sham (K-S) orbital. The ground-state energy ($E[\rho]$) in DFT is

$$E[\rho] = T_s[\rho] + \int V_{ext}(r)\rho(r)\, dr + E_H[\rho] + E_{XC}[\rho] \tag{2-4}$$

In equation 1-2, $T_s[\rho]$ is the K-S kinetic energy represents the sum of the kinetic energies of non-interacting electrons, V_{ext} is the external potential representing the interaction between an electron and the nuclei, E_H is the potential representing the interaction between an electron with electron density determined by other electrons, and E_{XC} represents the exchange-correlation energy. In

short, E_{XC} is comprised of the energy released when electrons with same spin exchange their positions and the energy gained when an atom moving under the influence of other electrons.

E_{XC} is the only part in K-S equation that requires effective approximations due to being mathematically undefined. The first approximation used in K-S DFT calculation is Local-Density Approximation (LDA) assuming the exchange correlation energy is same regardless of the position in the system. Generalized Gradient Approximation (GGA) is an approximation which considers both local electron density and its gradient[44], and that makes GGA more reliable than LDA. Perdew-Burke-Ernzerhof (PBE) functional is a commonly used GGA functional which we used in this research, which can calculate the properties of metal compounds accurately[45]. We implement the K-S DFT calculations by using the CP2K package that performs atomistic simulation of solid state, liquid, molecular, and biological systems.

2.2 Genetic Programming

Fundamentally, symbolic regression is the creation of equations by combining functions, operators, and variables. For convenience in generating and modifying equations algorithmically, they are typically represented as trees (see Figure S1 for an example of a function represented as a tree). Unfortunately, because it is not restricted to linear combinations of descriptors (which would be linear regression), symbolic regression poses an NP (as in Non-Polynomial time) - hard optimization problem[55]. Oftentimes, a genetic algorithm is used as the optimization algorithm in the case of symbolic regression. This combination of symbolic regression and genetic algorithm is actually a type of genetic programming[56]. In genetic programming, a population of programs (in our case, a tree representation of a function) are randomly generated, and evaluated with a training

set to measure its fitness. Programs will be selected for future generation base on their fitness. When the next generation is reached, the programs are either kept the same or modified using methods such as reproduction, crossover, or mutation to form a new population. Over time, the programs tend stochastically toward the best fitness[57].

In this study we use the implementation of genetic programming given by Eureqa[58]. In addition to its genetic programming capabilities, Eureqa tries to assess the complexity of each model generated, by supplying a complexity value to each operator (for example, the natural logarithm may receive a value of 3, whereas the addition operator may receive a value of 1) and reporting the sum total of an equation's complexity values. For example, $\ln(x)$ would have a lower complexity score than $\ln(x^2)$, due to the presence of an additional operation (taking the square of x) in the latter. At each complexity level, it reports the best-fitting equation it has found.

3.0 Results and Discussion

In this part, we first select the suitable metals, supports, surface facets, and sites to investigate the MSIs of metals on supports. We choose them to screen the physical properties of metal-support pairs and understand the origins of SAC stabilization. After adding single metal atoms on the sites of support facets we select, we calculate the corresponding adsorption energies of metals on supports by DFT calculations, and observe the final structures after optimization.

Next we plot the adsorption trend of metals on supports to retrieve the relationship between adsorption energy and the metal-support pairs. We determine two descriptors of adsorption energy, which are metal-oxygen binding energy in gas phase and band gap of the oxide support. Then we utilize the DFT calculation results as training set for genetic programming. We develop a predictive model that can predict the adsorption energy of metals on supports.

Finally, we apply the Square-Root Bond (SRB) cutting model[59-60] to introduce a hypothetical cohesive energy of metal nanoparticles. We plot the hypothetical cohesive energy versus the DFT calculated metal adsorption energy. Based on this plot, we introduce a guiding principle to hypothesize the synthetic accessibility of SACs based on the balance between metal adsorption on support and cohesion of metal nanoparticles.

3.1 The Selection of Metals, Supports, Surface Facets, and Sites

In this work, we studied the MSIs of single metal atoms spanning different columns and rows in the periodic table (Au, Cu, Ag, Pt, Pd, Ni, Rh, Ir) on γ-Al_2O_3, MgO, and $MgAl_2O_4$, which are both thermally stable and commonly used as supports in catalysis[61-63]. In these oxides, the surface Lewis acid-base properties for under-coordinated site pairs enable charge transfer when metal atoms adsorb on the surface[64-67]. Because of their ubiquity as supports, a series of SACs have already been synthesized on them, including Pt_1/γ-Al_2O_3[68], Rh_1/γ-Al_2O_3[25, 69], Au_1/MgO[70], Pd_1/MgO[36], and $Ir_1/MgAl_2O_4$[71].

Different surface facets of metal oxides exhibit different surface coordination, so we investigate some low-index surface facets: γ-Al_2O_3 (100), γ-Al_2O_3 (110), γ-Al_2O_3 (111), MgO (100), MgO (110), $MgAl_2O_4$ (100), and $MgAl_2O_4$ (110). Depending on the offset of the termination plane from the origin of the unit cell, each crystallographic facet can be terminated with different atoms. Therefore, we screen multiple surface terminations for each facet and report the most thermodynamically-stable surfaces since they likely represent a significant portion of the exposed surface area. The MgO (111) and $MgAl_2O_4$ (111) surfaces exhibit high net dipole due to their asymmetric nature, which results in high energy regardless of termination. In addition, they undergo severe restructuring (indicative of unstable surfaces), so we do not include them in this study. The optimized bulk structures and the most stable facets of the rest of the considered oxide supports are shown in Figure 1. The other facets are shown in Figure S2.

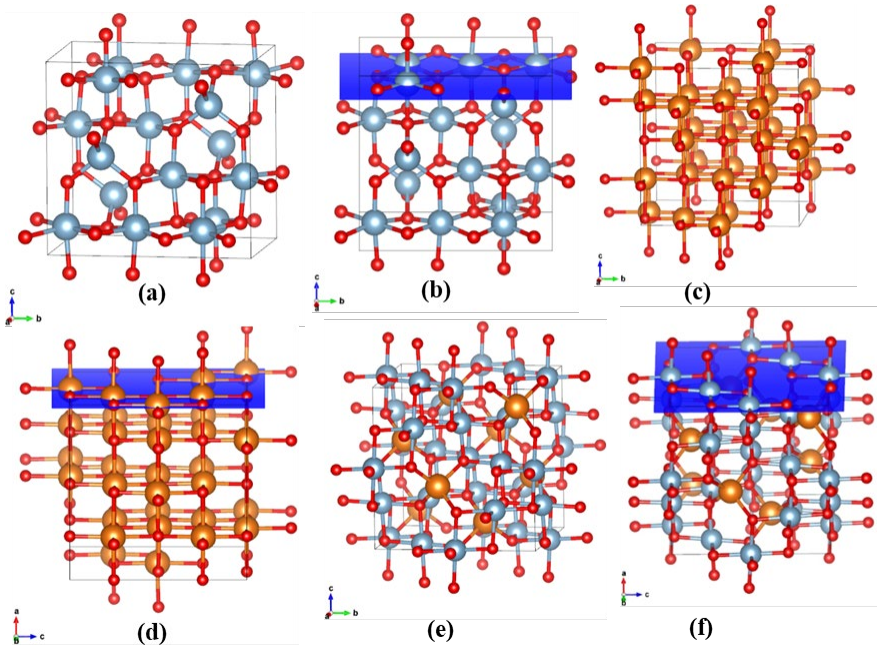

Figure 1 Structures of (a) γ-Al_2O_3 bulk, (b) γ-Al_2O_3 (100) surface plane, (c) MgO bulk, (d) MgO (100) surface plane, (e) $MgAl_2O_4$ bulk, and (f) $MgAl_2O_4$ (100) surface plane. The surface cleaving plane is highlighted in blue. Orange atoms represent Mg, grey atoms represent Al, and red atoms represent O.

Following optimization of the different surfaces, we placed single metal atoms on different sites. Depending on the surface heterogeneity of the oxide surface, several metal adsorption sites may be possible. The initial guess for the metal adsorption site is selected to maximize the interaction of metal atom with neighboring surface oxygen atoms, because many of the metal atoms we select are oxophilic in nature. We investigate 4 adsorption sites each on γ-Al_2O_3 (100) and (111) (Figure 2a, 2c), 5 sites on γ-Al_2O_3 (110) (Figure 2b), 1 site each on MgO (100) and (110) (Figure 2d, 2e), 3 sites on $MgAl_2O_4$ (100) (Figure 2f), and 2 sites on $MgAl_2O_4$ (110) (Figure 2g). Overall, this allows us to include a large variety of adsorption sites in our dataset.

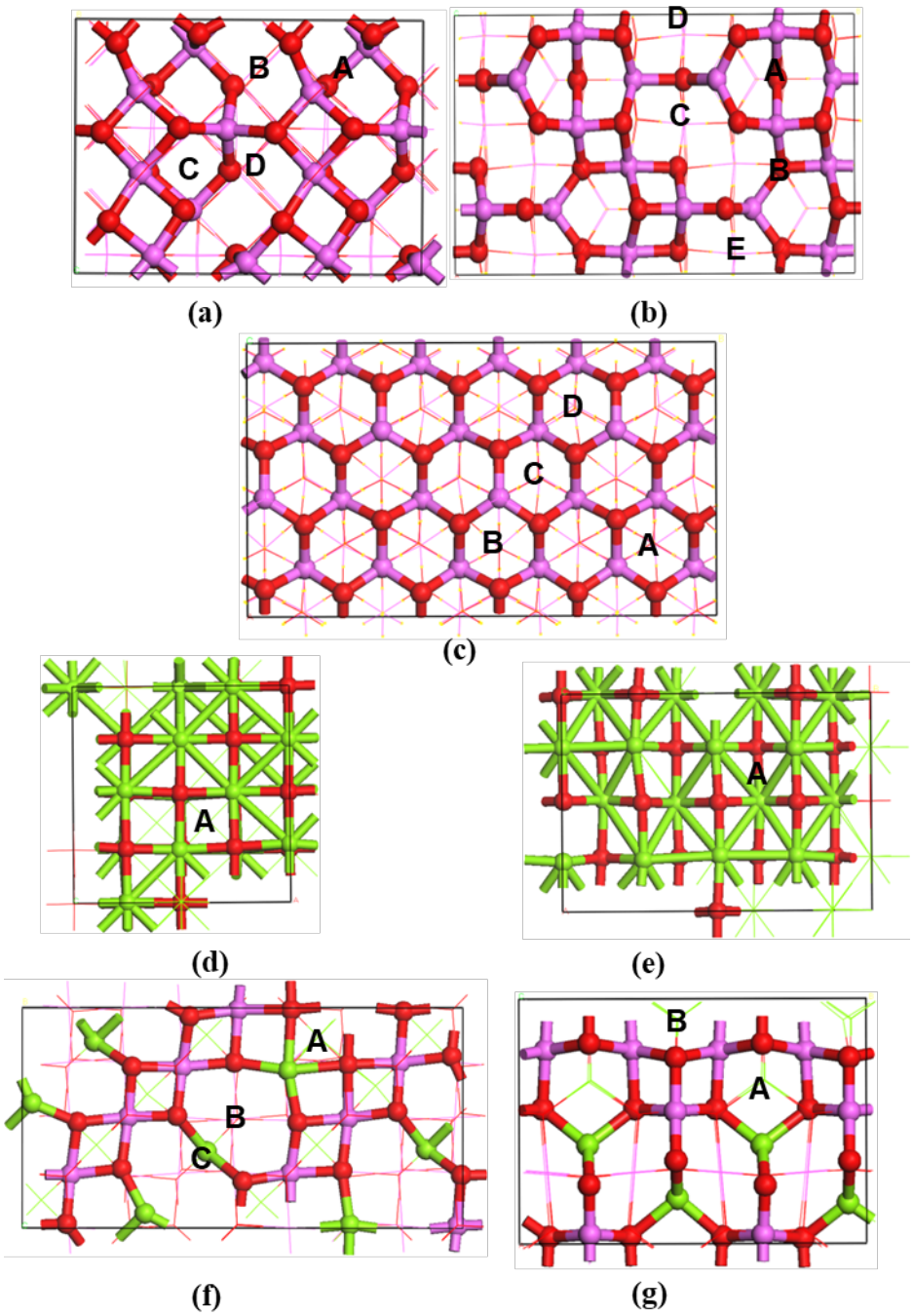

Figure 2 Chosen sites on the lowest energy termination of (a) γ-Al_2O_3 (100), (b) γ-Al_2O_3 (110), (c) γ-Al_2O_3 (111), (d) MgO (100), (e) MgO (110), (f) $MgAl_2O_4$ (100), and (g) $MgAl_2O_4$ (110). Sites are indicated with capital letters. Only top layers are shown by ball-and-stick, the atoms in the subsurface are shown by a wireframe. Green atoms represent Mg, pink atoms represent Al, and red atoms represent O.

3.2 Preferred Adsorption Sites of Metals on Supports

On γ-Al_2O_3 (100), the preferred adsorption configuration for all metal atoms except Cu is a hollow site between two oxygens (Figure 3a, 3b), while Cu is in a hollow site between two different oxygens (Figure 3c). The metal atoms coordinate with both Al and O atoms. The DFT-calculated adsorption energies are as follows: Pt (E_{ads} = -4.62 eV) < Ir (E_{ads} = -4.56 eV) < Rh (E_{ads} = -3.57 eV) < Ni (E_{ads} = -3.55 eV) < Pd (E_{ads} = -2.59 eV) < Cu (E_{ads} = -1.64 eV) < Au (E_{ads} = -0.97 eV) < Ag (E_{ads} = -0.79 eV). By convention, more negative adsorption energies are stronger. Additional details regarding the geometry of the binding sites can be found in Table S4.

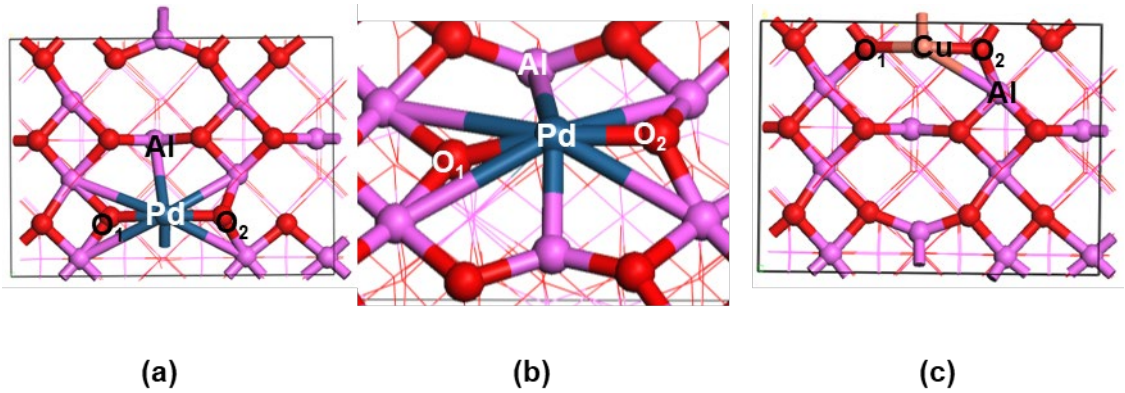

Figure 3 Pd adsorption on γ-Al_2O_3 (100) in (a) top, (b) side view and Cu adsorption on γ-Al_2O_3 (100) in (c) top view. The copper atom represents Cu, blue atoms represent Pt, pink atoms represent Al, and red atoms represent O.

On γ-Al_2O_3 (110) the strongest adsorption site for Au is a hollow site between Al and O atoms (Figure 4a, 4b), Cu binds in the same configuration. Ag prefers adsorption in a hollow site between a different pair of Al and O atoms (Figure S3a, S3b). Pd adsorbs to a hollow site which

is close to the adsorption site of Au and Cu (Figure S3c, S3d). Pt prefers a different hollow site (Figure 4c, 4d), while Ni, Rh, and Ir bind in an identical configuration. The DFT-calculated metal adsorption energies follow Ir (E_{ads} = -3.87 eV) < Pt (E_{ads} = -3.71 eV) < Ni (E_{ads} = -3.14 eV) < Rh (E_{ads} = -2.69 eV) < Pd (E_{ads} = -2.20 eV) < Cu (E_{ads} = -1.64 eV) < Au (E_{ads} = -1.49 eV) < Ag (E_{ads} = -1.18 eV). We note that the strong adsorptions (Pt, Ni, Rh, and Ir) cause surface restructuring on the surface facet (Figure 4e, 4f).

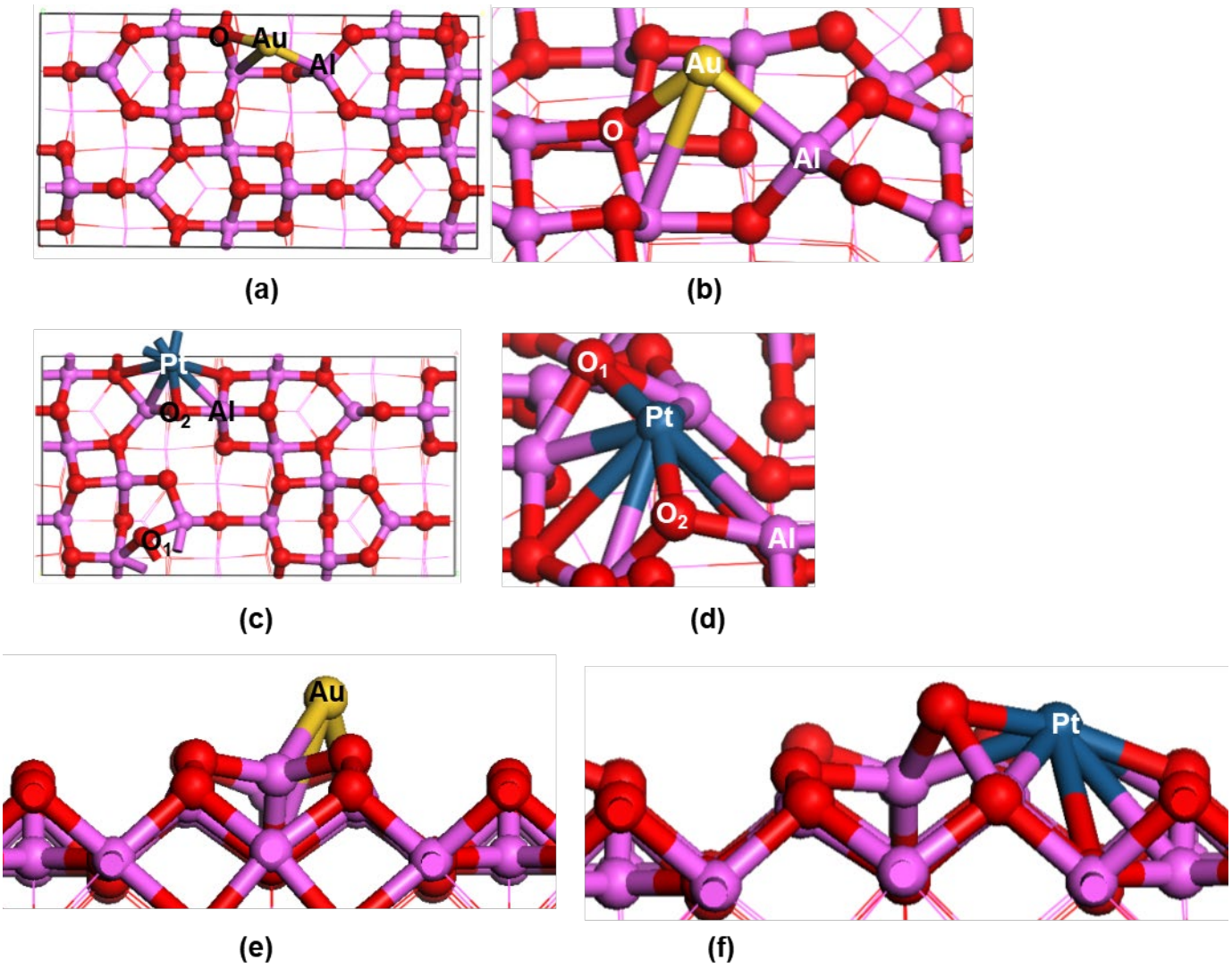

Figure 4 Au adsorption on γ-Al_2O_3 (110) (a) top view, (b) side view; Pt adsorption on γ-Al_2O_3 (110) (c) top view, (d) side view. Surface restructuring is observed by comparing side views of the γ-Al_2O_3 (110) support surface when interacting with (e) Au and (f) Pt. Yellow atoms represent Au, blue atoms represent Pt, pink atoms represent Al, and red atoms represent O.

On γ-Al_2O_3 (111), metals bind on the hollow site (Figure 5c, 5d). The DFT-calculated metal adsorption energies are Ir (E_{ads} = -8.25 eV) < Ni (E_{ads} = -8.04 eV) < Rh (E_{ads} = -7.36 eV) < Pt (E_{ads} = -6.35 eV) < Cu (E_{ads} = -5.96 eV) < Pd (E_{ads} = -5.13 eV) < Ag (E_{ads} = -4.54 eV) < Au (E_{ads} = -

3.75 eV). For the relatively weak-binding metals Ag, they bind in a different hollow site from the stronger-binding metals Pt (Figure 5a, 5b). The binding configuration for Au is same as Ag. Cu, Pd, Ni, Rh, and Ir bind in the identical configuration.

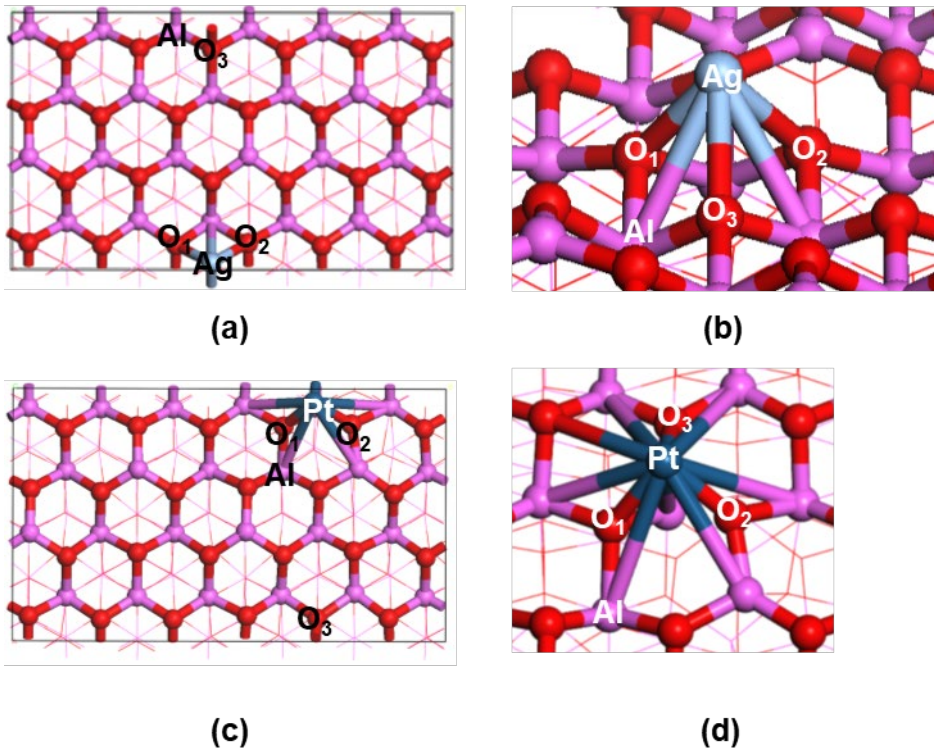

Figure 5 Ag adsorption on γ-Al_2O_3 (111) in (a) top view, (b) side view; Pt adsorption on γ-Al_2O_3 (111) in (c) top view, (d) side view. Grey atoms represent Ag, blue atoms represent Pt, pink atoms represent Al, and red atoms represent O.

The slab model of MgO (100) yields a highly symmetric support structure. We note that metals adsorb directly above an oxygen atom and coordinate with several neighboring Mg atoms (Figure 6a, 6b). Rh prefers to bind in a hollow site (Figure 6c, 6d), and Ir binds in the same configuration. The DFT-calculated adsorption energies are: Pt (E_{ads} = -3.07 eV) < Ir (E_{ads} = -2.56

eV) < Rh (E_{ads} = -2.03 eV) < Ni (E_{ads} = -1.98 eV) < Pd (E_{ads} = -1.68 eV) < Au (E_{ads} = -1.08 eV) < Cu (E_{ads} = -0.98 eV) < Ag (E_{ads} = -0.68 eV).

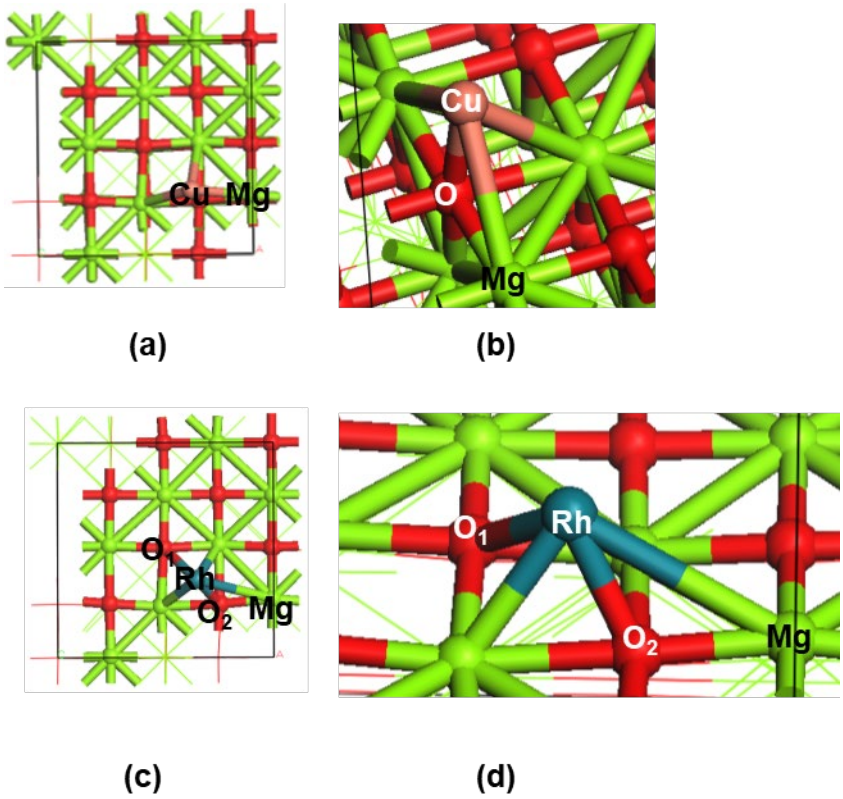

Figure 6 Cu adsorption on MgO (100) from (a) top view, (b) side view; Rh adsorption on MgO (100) from the respective (c) top view, (d) side view. Copper atoms represent Cu, blue atoms represent Rh, green atoms represent Mg, and red atoms represent O.

On the other stable surface facet of MgO, the (110), most metals strongly bind in a hollow site between two oxygen atoms and coordinate with several nearby Mg atoms (Figure 7a, 7b). The most-favorable binding site for Pt is slightly different, instead preferring a site directly above an

oxygen and coordinates nearby O and Mg atoms (Figure 7c, 7d). The DFT-calculated metal adsorption energy is as follows: Ir (E_{ads} = -4.73 eV) < Pt (E_{ads} = -4.48 eV) < Ni (E_{ads} = -3.84 eV) < Rh (E_{ads} = -3.78 eV) < Cu (E_{ads} = -2.57 eV) < Pd (E_{ads} = -2.54 eV) < Au (E_{ads} = -2.10 eV) < Ag (E_{ads} = -2.08 eV).

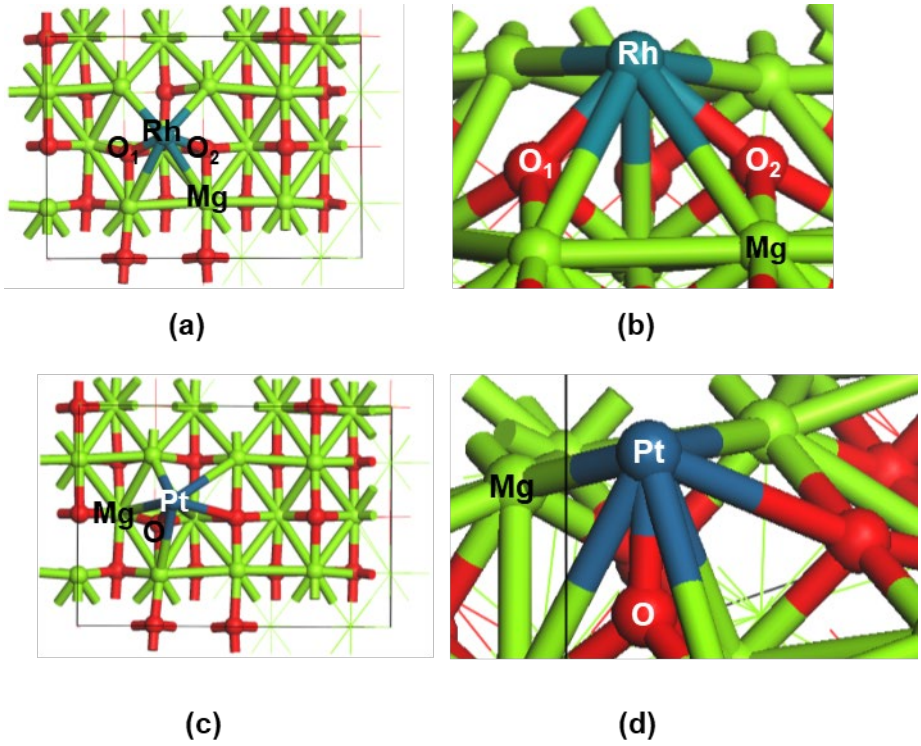

Figure 7 Rh adsorption on MgO (110) in (a) top view, (b) side view; Pt adsorption on MgO (110) in (c) top view, (d) side view. Light blue atoms represent Rh, dark atoms represent Pt, green atoms represent Mg, and red atoms represent O.

Due to the lower symmetry of $MgAl_2O_4$ (100), the observed adsorption behavior of different metals varies. Au and Cu bridge the same two nearby Mg atoms (Figure S4), the binding configuration of Ag is the same as Au. Pt adsorption in a hollow site while coordinating with neighboring Mg, Al, and O atoms (Figure 8a, 8b), Pd and Ni bind on the identical configuration.

Rh is in a different hollow site between two oxygens and coordinating with nearby Mg, Al atoms (Figure 8c, 8d), while the binding configuration of Ir is the same as Rh. The DFT-calculated metal adsorption energies are: Pt (E_{ads} = -3.89 eV) < Ir (E_{ads} = -3.61 eV) < Ni (E_{ads} = -2.94 eV) < Rh (E_{ads} = -2.76 eV) < Au (E_{ads} = -2.38 eV) < Cu (E_{ads} = -1.81 eV) < Pd (E_{ads} = -1.81 eV) < Ag (E_{ads} = -1.21 eV).

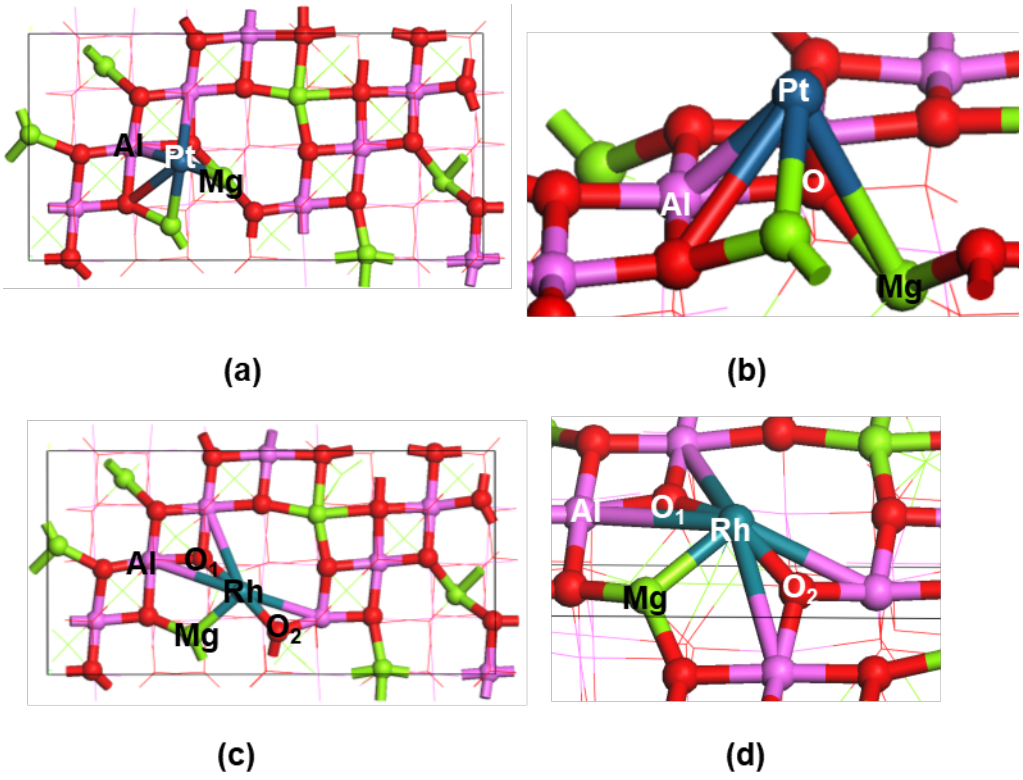

Figure 8 Pt adsorption on $MgAl_2O_4$ (100) (a) top view, (b) side view; Rh adsorption on $MgAl_2O_4$ (100) (c) top view, (d) side view. Dark blue atoms represent Pt, light blue atoms represent Rh, green atoms represent Mg, pink atoms represent Al, and red atoms represent O.

On $MgAl_2O_4$ (110), the strongest adsorption site for all metals are similar, which is a hollow site between two nearby oxygens on the surface (Figure 9). DFT-calculated metal adsorption energies are as follows: Ir (Eads = -7.34 eV) < Ni (E_{ads} = -6.18 eV) < Pt (E_{ads} = -5.77 eV) < Rh (E_{ads} = -5.50 eV) < Cu (E_{ads} = -4.78 eV) < Pd (E_{ads} = -3.74 eV) < Ag (E_{ads} = -3.25 eV) < Au (E_{ads} = -3.24 eV). Although their binding sites are similar, due to initially high surface energy of $MgAl_2O_4$ (110), the strong Ir adsorption resulted in a significant surface restructuring (Figure 9c, 9d).

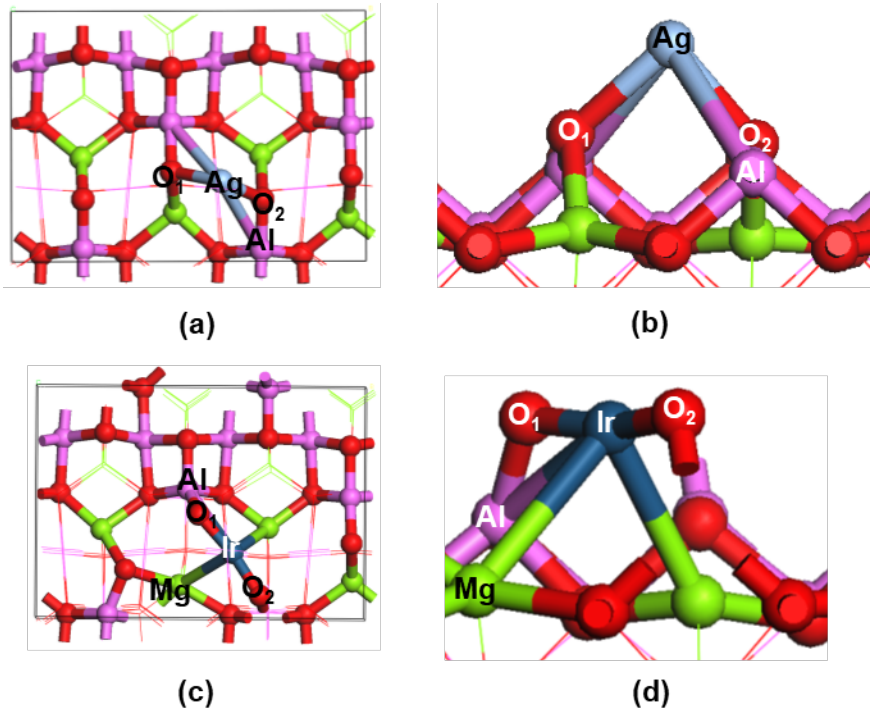

Figure 9 Ag adsorption on $MgAl_2O_4$ (110) in (a) top view, (b) side view; Ir adsorption on $MgAl_2O_4$ (110) in (c) top view, (d) side view. Grey atoms represent Ag, blue atoms represent Ir, green atoms represent Mg, pink atoms represent Al, and red atoms represent O.

Overall, we note that (i) metals are closer to oxygens after optimization. In the case of Ni adsorption on MgO (100), the initial placement of Ni is in a hollow site coordinate with nearby two Mg and 2 oxygens with average Ni-O distance 2.042 Å (Figure 10a). During DFT calculation, Ni atom moves toward the on-top site of an oxygen with final Ni-O distance 1.805 Å (Figure 10b). This suggests that the metal-oxygen binding is crucial for metal adsorption; (ii) strong MSIs (Pt/Ni/Rh/Ir on γ-Al_2O_3 (110) and Ir on $MgAl_2O_4$ (110)) induce surface restructuring in order to accommodate guest metals appropriately on the surface. During restructuring oxygen atoms which are initially close to the surface (Figure 9b) move away from the surface towards the supported metal (Figure 9d).

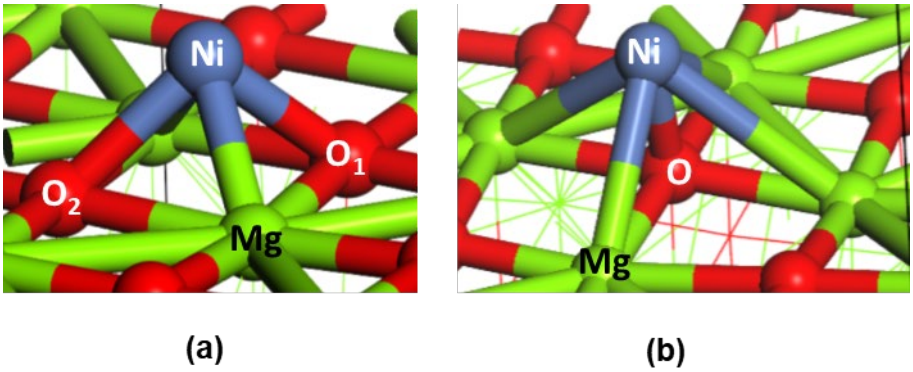

Figure 10 (a) Initial placement of Ni on MgO (100), (b) Ni adsorption on MgO (100) after optimization. Light blue atoms represent Ni, green atoms represent Mg, and red atoms represent O.

3.3 Adsorption Trend of Metals on Supports

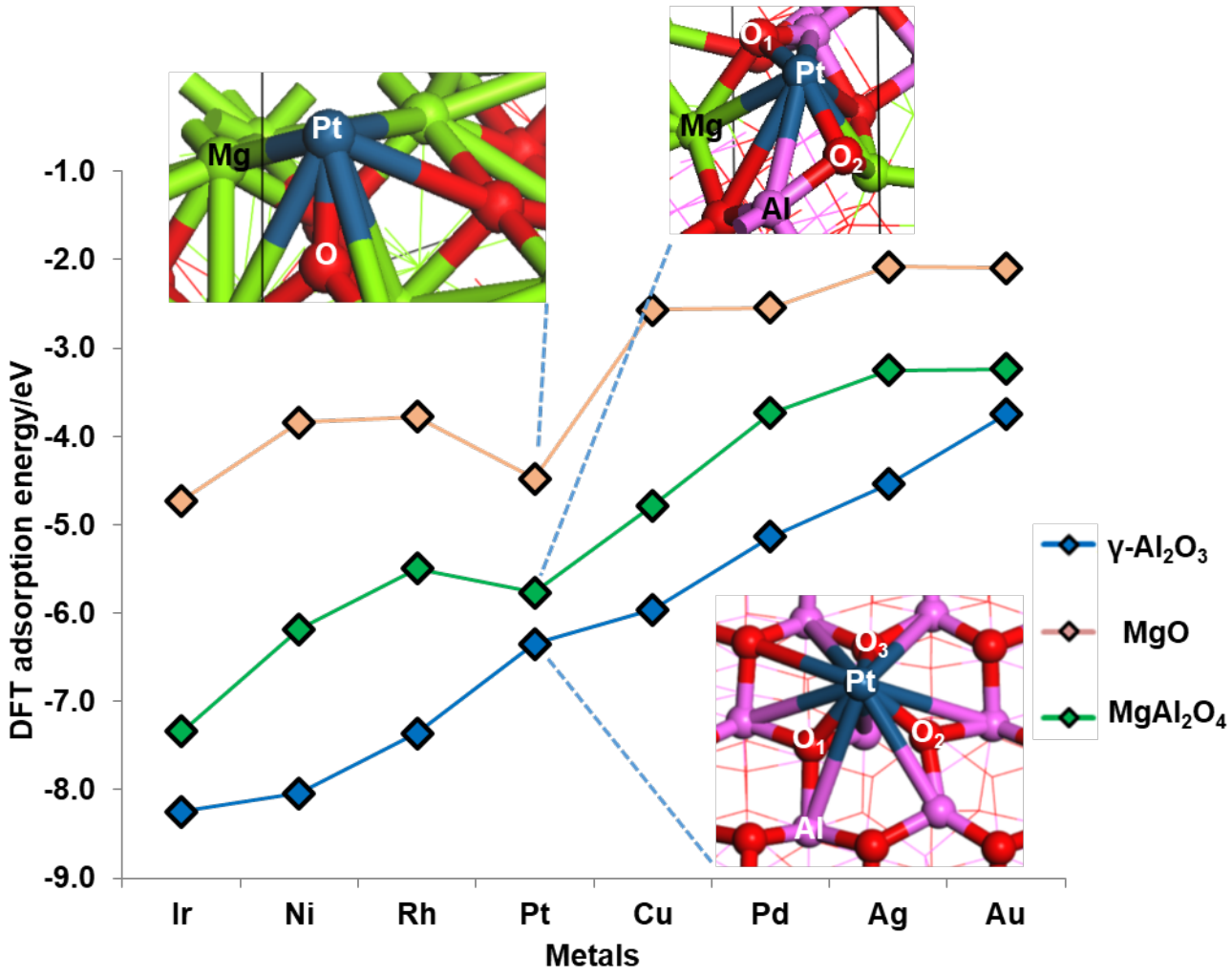

Figure 11 The DFT-calculated metal adsorption energy for most preferred sites of different transition metals adsorbed on different supports; the structures of Pt adsorption are attached for an insight in the structures. Blue atoms represent Pt, green atoms represent Mg, pink atoms represent Al, and red atoms represent O.

In Figure 11, we plot the adsorption energy of metals in their most preferred sites on different oxide supports in order to compare their adsorption behavior. We observe for every metal,

the metal adsorption is strongest on γ-Al_2O_3 and weakest on MgO. The metal adsorption on $MgAl_2O_4$ is between γ-Al_2O_3 and MgO while the chemical formula of $MgAl_2O_4$ is the combination of Al_2O_3 and MgO. Because of the similarity in adsorption energy trends for every metal, this suggests that if a metal strongly adsorbs to γ-Al_2O_3, it would also adsorb on MgO and $MgAl_2O_4$ with a stronger interaction compared to the other metals, Ir always binds strongest among the metals we choose for instance. These highlighting the role of both the metal and support in governing the overall MSIs.

3.4 Descriptors of Metal Adsorption Energy

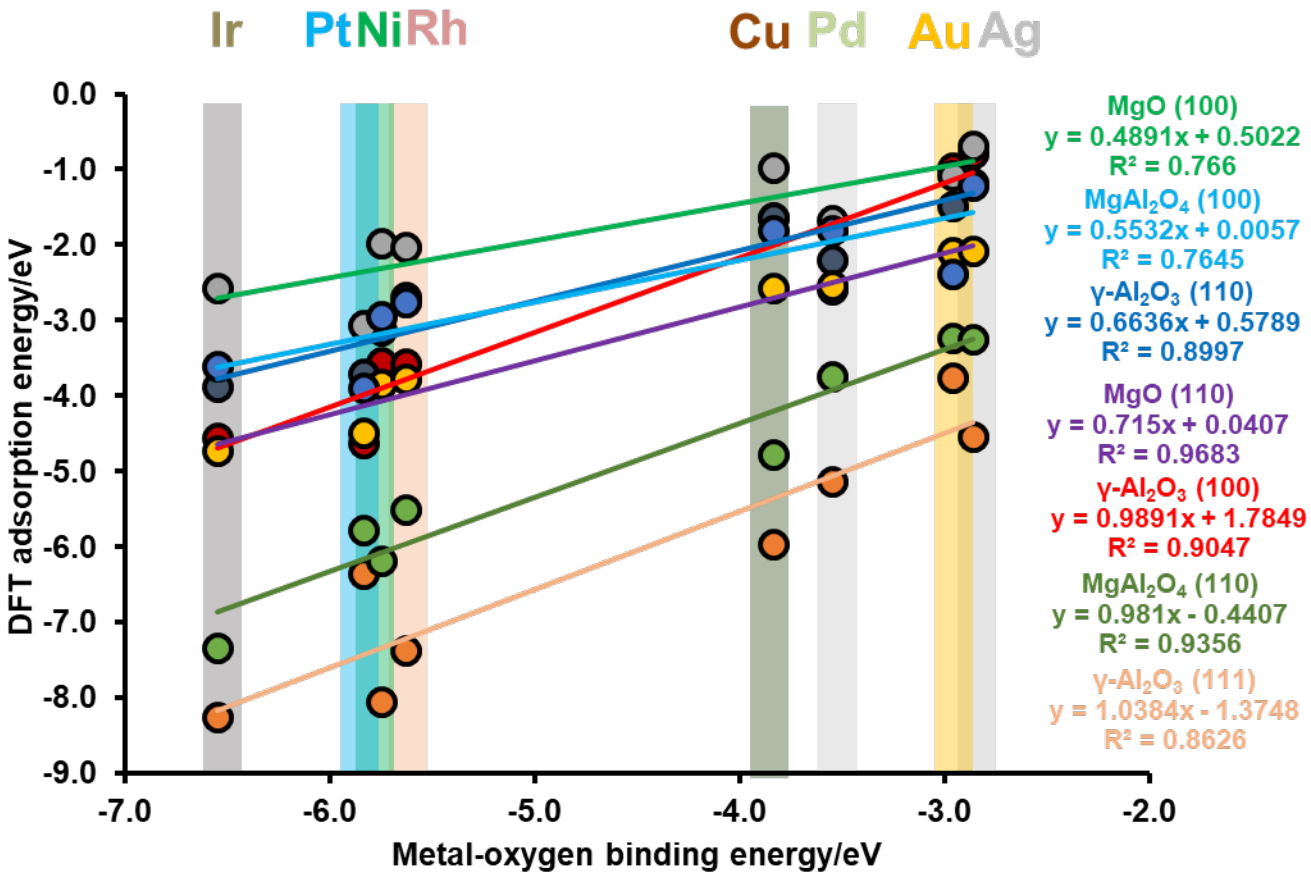

Figure 12 Relationships between DFT-calculated metal adsorption energy on each surface facet and metal-oxygen binding energy of the supported SAC.

To solidify our conclusions regarding the relationship between the metal-oxygen binding and the MSI, in Figure 12 we plot the adsorption energy of the most preferred site for each metal on several different surface facets versus the metal-oxygen binding energy ($E_{M\text{-}O}$). $E_{M\text{-}O}$ refers to the calculated binding energy of a single metal atom with a single oxygen atom in the gas phase

(Table S3c). We observe a linear relationship between the metal's adsorption energy on its preferred site of the support and the corresponding E_{M-O}: the stronger the E_{M-O} in the gas phase, the stronger the adsorption energy to the support. On all the considered facets of γ-Al_2O_3, the relationship between metal adsorption energy and E_{M-O} is strong. One of the reasons for this relationship is that except for the relatively weaker-binding cases of Au/Cu/Ag on γ-Al_2O_3 (110) (Figure 4a, 4b and Figure S3a, S3b), all preferred sites for metals on γ-Al_2O_3 are found to coordinate with a number of oxygen atoms. As a result, the metal-oxygen interaction becomes a major factor for adsorption on γ-Al_2O_3, which E_{M-O} characterizes. The correlation between metal adsorption energy and E_{M-O} on MgO (100) is weaker due to most metals only coordinating with one oxygen (Figure 6a, 6b). On MgO (110) every metal participates in strong bonds with two oxygens (Figure S7) and as a result E_{M-O} works well as a descriptor. On $MgAl_2O_4$ (100), Au, Cu, and Ag do not form any bond with oxygen on the support (Figure S4) and the correlation between metal adsorption energy and E_{M-O} is low. On $MgAl_2O_4$ (110), the correlation is excellent due to a higher metal-oxygen coordination compares with $MgAl_2O_4$ (100) (Figure 9). To summarize, E_{M-O} is correlated with MSIs on oxide supports and is useful as a descriptor for metal adsorption energy when the metal is expected to bind with oxygen atoms.

We now search for a descriptor based on the properties of support, because it is also an important aspect of the adsorption interaction (see our discussion of Figure 11). However, this is not straightforward because the supports display complex structures which occasionally reconstruct during metal adsorption. After screening several support properties (surface energy, band gap, ionization potential, and fermi energy), we identified the support band gap correlates best with metal adsorption energy. We plot the adsorption energy of metal atoms on the most preferred site versus the band gap of the support in Figure 13. We note that the smaller the band

gap the stronger the adsorption. This makes sense, because adsorption of metals on supports involves charge transfer[19]. A support with a low band gap can more-easily transfer electron density to form bonds with the adsorbed metal atom, enhancing the adsorption interaction[72].

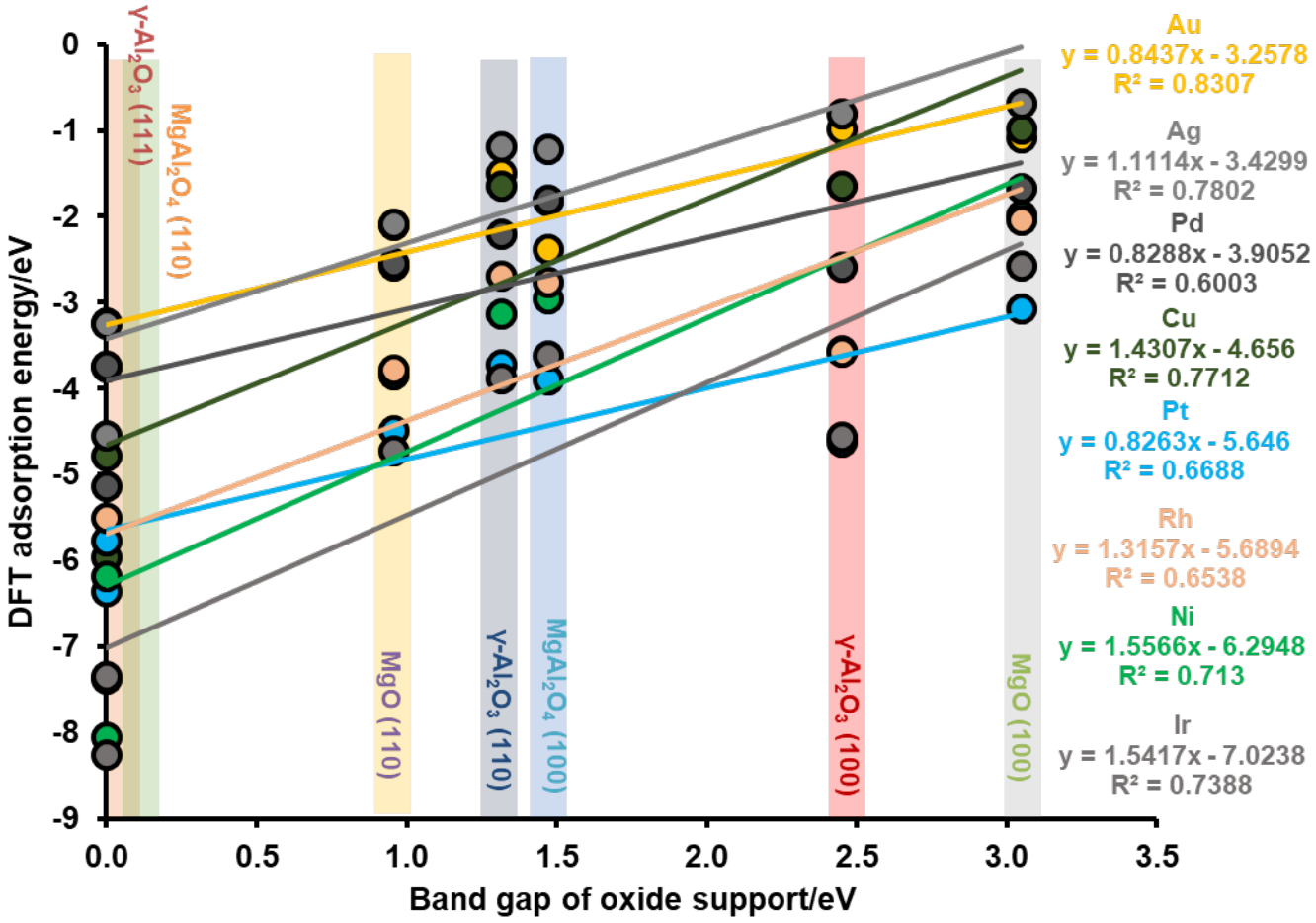

Figure 13 Relationship between DFT metal adsorption energy and band gap of the oxide support.

3.5 Predictive Model of Metal Adsorption Energy

The adsorption of metal atoms on the oxide supports involves complex MSIs. As a result, we suspect that additional nonlinear factors may play a role on describing adsorption. To explore possibly nonlinear factors related to the MSI, we employ symbolic regression via genetic programming as implemented in Eureqa[58].

The training set consists of our DFT-calculated adsorption energies, along with several possible physical descriptors which are obtained from literature and our own calculations. We calculate the following descriptors using DFT: gas-phase metal-oxygen binding energy ($E_{M\text{-}O}$), ionization potential of the support, band gap of the support, Fermi energy of the oxide support, gas-phase HOMO-LUMO gap of the metal, gas-phase Fermi energy of metal, and surface energy of the support (more details are given in Table S3c, S3d, S3e, S3f). In addition to the DFT-calculated parameters, we also investigate coordination numbers (using the Van der Waals radii reported in Table S5). We also use a "hypothetical cohesive energy" (CE_{hyp}) described in the SRB cutting model to predict metal nanoparticle energetics in SACs[59-60]. This is given in Equation 3-1, where CE_{bulk} is the experimental cohesive energy for metals in the bulk, CN is the total coordination between the supported metal atom and support; CN_{bulk} is the metal atom's coordination number in its own bulk. Because we only investigate FCC metals, CN_{bulk} is always 12. We assume the metal cohesive energy on the support is the cohesive energy of metal on its own metal slab while the coordination number is the same as the metal adsorption on the support.

$$CE_{hyp} = CE_{bulk}\sqrt{\frac{CN}{CN_{bulk}}} \tag{3-1}$$

We take the following physical properties for the metal from literature: experimental bulk cohesive energy[73], experimental ionization potential[74], experimental electron affinity[74], oxidation enthalpy[19], Van del Waal radius[75-76], electron configuration[74], Martynov–Batsanov electronegativity[19], covalent radius of a triple bond[77], heat of vaporization[78], and electrical resistivity at 273 K[74] (Table S3a, S3b).

In order to combat overfitting, we take 5 subsamples of the dataset, consisting of only 75% of the total dataset, and use each as separate training sets. Genetic programming is inherently a stochastic process, so we run it multiple times to have confidence on our results. For each training set we run Eureqa 5 times (25 searches total), halting each search after 2 million generations. The complexity is assessed on the equation generated by the genetic algorithm. We plot in Figure S6 the Pareto Front[56] (the set of equations for each complexity which minimize the error) of equations generated by Eureqa, using the RMSE reported by Eureqa.

The equations generated by Eureqa don't necessarily have their coefficients optimized, as they are generated with a genetic algorithm. To further reduce the error of the beset equations found by Eureqa, we optimize their coefficients using the Simplex method of Nelder and Mead[79] as implemented in the *optim* function in R. To ensure accurate estimates of RMSE, we utilize bootstrapping (i.e. sampling with replacement from the dataset). We take a bootstrap sample, then optimize the coefficients. The RMSE is then recorded and another round of sampling and

optimization is performed. We repeat this process of bootstrap sampling and optimization 10,000 times for each function. The results of this method are provided in Table S6. Finally, we use the whole (un-bootstrapped) dataset and optimize its coefficients to generate Equation 3-2. Equation 3-2 is the best equation in terms of bootstrapped RMSE, equaling 0.69 eV. E_{ads} is metal adsorption energy, $E_{M\text{-}O}$ represents the gas-phase metal-oxygen binding energy of supported metal, IP_s represents the ionization potential of the oxide support, and BG_s represents the band gap of the oxide support.

$$E_{ads} = 0.523 * E_{M-O} + \frac{0.413 * E_{M-O} - 1.243 * IP_s - 4.147}{4.740 * BG_s + 1.165} + 0.859 \quad (3\text{-}2)$$

The correlation between DFT adsorption energy in our data set and hypothetical adsorption energy calculated using Equation 3-2 is show in Figure 14.

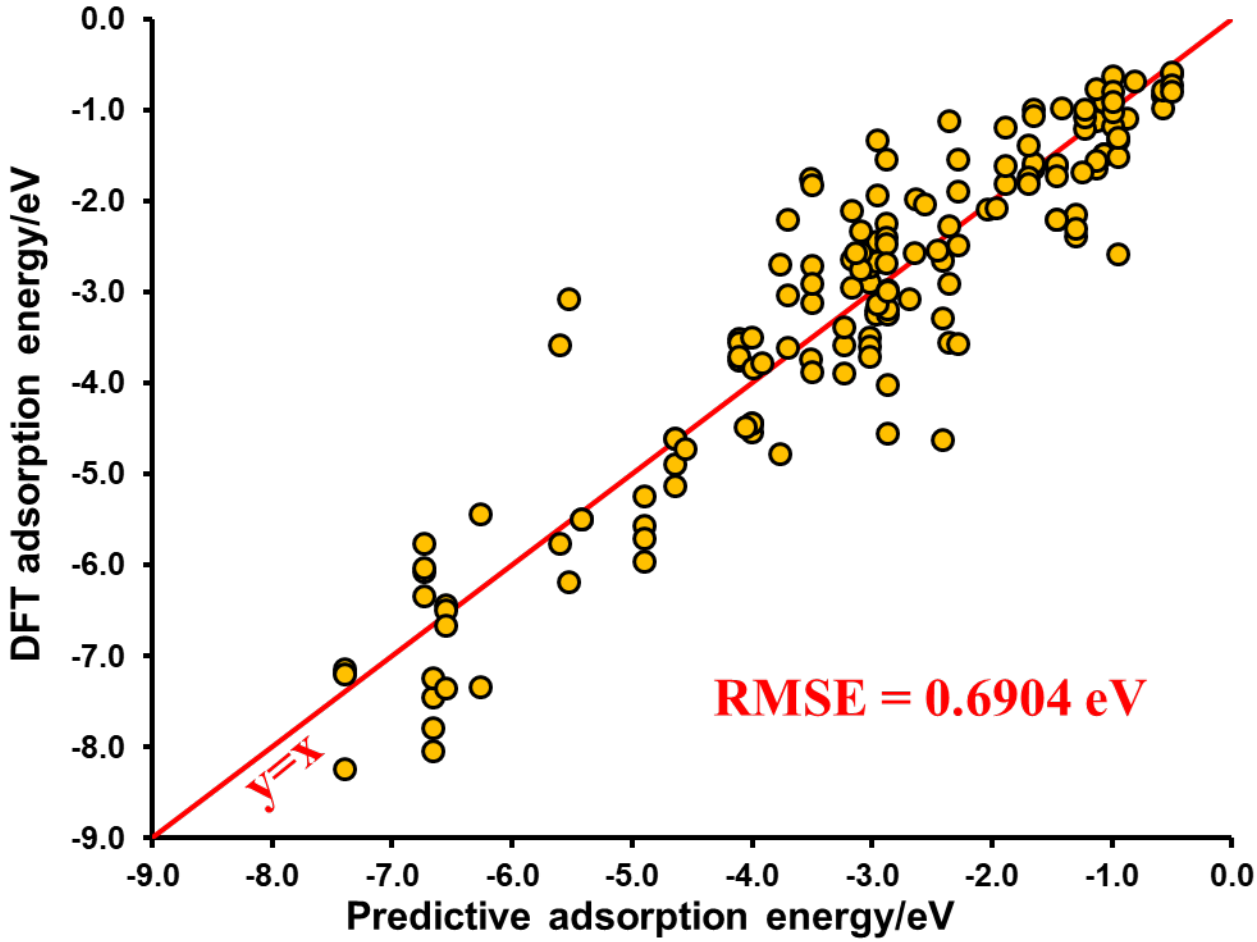

Figure 14 DFT adsorption energy versus predictive adsorption energy calculated by Equation 3-2.

Overall, this equation supports what we elucidated from our calculations. We have already shown the band gap of the oxide support (BG_s) and metal oxygen binding energy (E_{M-O}) strongly correlate with the metal adsorption energy. Furthermore, the inclusion of the ionization potential of the support (IP_s) supports our conclusion of charge transfer playing an important role in metal adsorption on support. Examining models recently reported by O'Connor et al[19], we find several similar descriptors: the oxide formation enthalpy of the metal (which is similar to our E_{M-O}), ratio of the LUMO of the support and metal (we use the support band gap, which is the LUMO –

HOMO), and electron affinity of the metal (we use ionization potential of the support) in particular stand out. Our bootstrapped RMSE equals 0.69, which indicates our model is better-suited to a coarse-grained approach to screen a large pool of potential metal-surface pairs before applying a more expensive technique such as DFT.

3.6 Hypothesize the Synthetic Accessibility of Single-Atom Catalysts

Stabilizing single metal atoms with a support is a necessity for the creation of stable (i.e. sintering-resistant) SACs. This manifests as a competition between the bulk cohesive energy of the metal atoms (which enhances sintering) and their binding energy with the support (which enhances atomic dispersion). From a thermodynamics perspective, if the strength of the MSI is stronger than the (pure) metal cohesive energy (in the same coordination environment), the single metal atom will energetically prefer adsorption to the support, stabilizing the SAC to resist sintering. We use the SRB model (Equation 3-1) to estimate the hypothetical cohesive energy (E_{hyp}) of the metal atom.

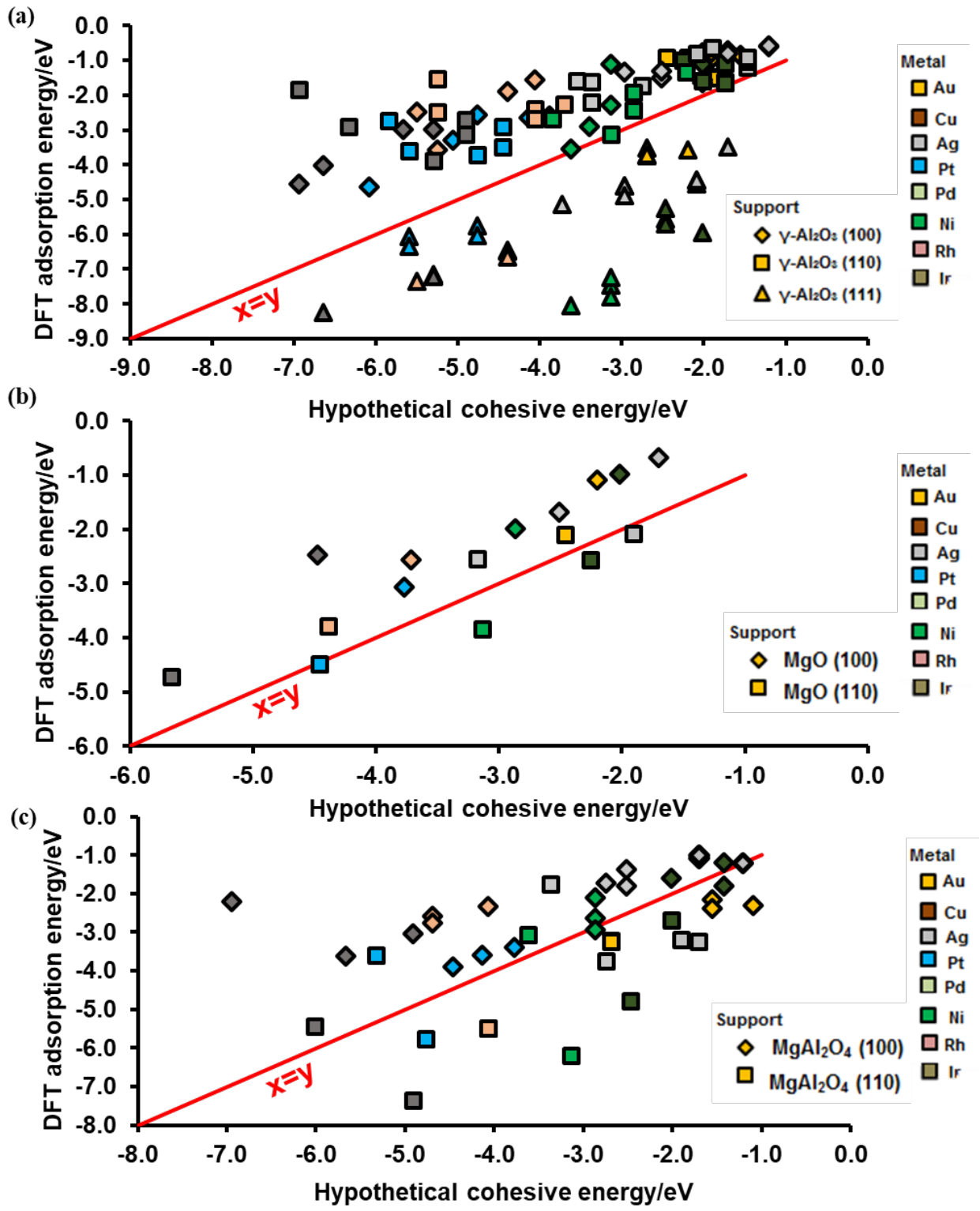

Figure 15 DFT adsorption energy vs hypothetical cohesive energy of supported metal on (a) γ-Al_2O_3 (b) MgO and (c) $MgAl_2O_4$.

In Figure 15 we plot the adsorption energy of the metal atoms on the different supports versus the E_{hyp} of the metal. In other words, we account for a hypothetical environment where the metal atom is in its own bulk with the same coordination that has on the support. With this formulation we are able to address the metal's atom preference to interact with the support or with its parent metal (in a cluster/nanoparticle). The red line shows the boundary where the supported metal adsorption energy is equal to SRB-calculated metal cohesive energy. The points below the red line indicate the adsorption energy is higher than cohesive energy of given metal atom, and the corresponding SACs formation is therefore suggested to be more favorable. We note that for γ-Al_2O_3 surface, all data points on (100) and (110) are above the red line, which suggests that stabilizing SACs on these facets may be difficult. However, on (111), all the considered metals are likely to yield stable SACs, as they are located below the red line (Figure 15a), showing a facet-specific thermodynamic preference for the formation of SACs. We notice that Pt and Rh SACs have already been synthesized on γ-Al_2O_3 [68-69]. Similarly, on MgO, the surface facet plays an important role in stabilizing SACs, and four points fall under the red line, which are Cu/Ag/Pt/Ni on MgO (110). Au/Pt/Pd/Rh/Ir SACs have already been synthesized on MgO[36, 61-63, 70]. It should be noticed that in Figure 15b, Au, Pd, Rh, and Ir on MgO (110) are also close to the red line, validating our predictions. On $MgAl_2O_4$, most of the data points for (110) surface facet sites are under the red line, suggesting that $MgAl_2O_4$ (110) could also be a good support for the formation of SACs (Figure 15c). Indeed, the Ir SAC has already been synthesized on $MgAl_2O_4$[71]. These results suggest that the balance between SRB based local metal atom cohesive energy and metal adsorption energy could be used as another rough indictor to hypothesize the stability of SACs.

4.0 Conclusions

In this work, we apply DFT and statistical methods to a series of transition metal atoms (Au, Cu, Ag, Pt, Pd, Ni, Rh, and Ir) supported on low-index surface facets of γ-Al_2O_3, MgO, and $MgAl_2O_4$ on a variety of sites in order to determine descriptors for SAC adsorption. Based on our DFT calculations, we identify two primary descriptors for MSIs: the binding energy of the metal-oxygen complex in the gas phase, and the band gap of the oxide support. By combining DFT calculations and a thorough statistical learning approach, we develop a mathematical model that is able to estimate MSIs in SACs. Moreover, we assess the stability of a number of SACs by comparing the DFT adsorption energy with a hypothetical metal atom cohesive energy (tendency of the metal to form clusters than be atomically dispersed on the support) calculated with the square root bond cutting model[59-60] of cohesive energy. Finally, this work introduces some guiding principles to hypothesize the synthetic accessibility of a number of SACs based on the balance between adsorption and cohesion of metal nanoparticles on supports.

Appendix A Example of CP2K Input Files

A.1 Input File (Example Al_2O_3 bulk optimization)

```
&GLOBAL
PRINT_LEVEL MEDIUM
PROJECT_NAME Al2O3
RUN_TYPE CELL_OPT
FLUSH_SHOULD_FLUSH T
&END GLOBAL
&MOTION
&GEO_OPT
TYPE MINIMIZATION
OPTIMIZER LBFGS
MAX_ITER 3000
MAX_DR 2.9999999999999997E-04
MAX_FORCE 4.5000000000000003E-05
RMS_DR 1.4999999999999999E-04
RMS_FORCE 3.0000000000000001E-05
&CG
MAX_STEEP_STEPS 0
&LINE_SEARCH
TYPE 2PNT
&END LINE_SEARCH
&END CG
&END GEO_OPT
&CELL_OPT
OPTIMIZER CG
MAX_ITER 1000
MAX_DR 3.0000000000000001E-03
MAX_FORCE 4.4999999999999999E-04
RMS_DR 1.5000000000000000E-03
RMS_FORCE 2.9999999999999997E-04
STEP_START_VAL 0
TYPE DIRECT_CELL_OPT
EXTERNAL_PRESSURE 1.0000000000000000E+00
KEEP_ANGLES T
PRESSURE_TOLERANCE 1.0000000000000000E+01
&CG
MAX_STEEP_STEPS 0
RESTART_LIMIT 9.4999999999999996E-01
```

```
&LINE_SEARCH
TYPE 2PNT
&END LINE_SEARCH
&END CG
&PRINT
&PROGRAM_RUN_INFO MEDIUM
&END PROGRAM_RUN_INFO
&CELL MEDIUM
&END CELL
&END PRINT
&END CELL_OPT
&END MOTION
&FORCE_EVAL
METHOD QS
STRESS_TENSOR ANALYTICAL
&DFT
BASIS_SET_FILE_NAME ./BASIS_MOLOPT
POTENTIAL_FILE_NAME ./GTH_POTENTIALS
CHARGE 0
&SCF
MAX_SCF 20
EPS_SCF 9.9999999999999995E-08
SCF_GUESS ATOMIC
&OT T
MINIMIZER DIIS
PRECONDITIONER FULL_ALL
ENERGY_GAP 1.0000000000000000E-03
&END OT
&OUTER_SCF T
EPS_SCF 9.9999999999999995E-08
&END OUTER_SCF
&END SCF
&QS
EPS_DEFAULT 9.9999999999999998E-13
&END QS
&MGRID
CUTOFF 4.0000000000000000E+02
&END MGRID
&XC
&XC_FUNCTIONAL PBE
&PBE
PARAMETRIZATION ORIG
&END PBE
&END XC_FUNCTIONAL
&VDW_POTENTIAL
DISPERSION_FUNCTIONAL PAIR_POTENTIAL
```

```
&PAIR_POTENTIAL
TYPE DFTD3
REFERENCE_FUNCTIONAL PBE
CALCULATE_C9_TERM .TRUE.
PARAMETER_FILE_NAME dftd3.dat
R_CUTOFF 15.0
VERBOSE_OUTPUT .TRUE.
&END PAIR_POTENTIAL
&END vdw_POTENTIAL
&END XC
&POISSON
POISSON_SOLVER PERIODIC
PERIODIC XYZ
&END POISSON
&END DFT
&SUBSYS
&CELL
A   5.58699989320000   0.00000000000000   0.00000000000000
B   0.00000000000000   8.41300010680000   0.00000000000000
C -0.08307778120000   0.00000000000000   8.06757209430000
PERIODIC XYZ
&END CELL
&TOPOLOGY
COORD_FILE_NAME final.xyz
COORDINATE XYZ
&END TOPOLOGY
&KIND Al
ELEMENT   Al
BASIS_SET DZVP-MOLOPT-SR-GTH-q3
POTENTIAL GTH-PBE-q3
&END KIND
&KIND O
ELEMENT   O
BASIS_SET TZVP-MOLOPT-GTH-q6
POTENTIAL GTH-PBE-q6
&END KIND
&KIND C
ELEMENT   C
BASIS_SET TZVP-MOLOPT-GTH-q4
POTENTIAL GTH-PBE-q4
&END KIND
&KIND H
ELEMENT   H
BASIS_SET TZVP-MOLOPT-GTH-q1
POTENTIAL GTH-PBE-q1
&END KIND
```

```
&KIND Mg
ELEMENT   Mg
BASIS_SET DZVP-MOLOPT-SR-GTH-q10
POTENTIAL GTH-PBE-q10
&END KIND
&END SUBSYS
&END FORCE_EVAL
```

A.2 Input File (Example Au adsorption on Al_2O_3 (100) site A)

```
&FORCE_EVAL
METHOD QS
&DFT
UKS T
RELAX_MULTIPLICITY
BASIS_SET_FILE_NAME BASIS_MOLOPT
POTENTIAL_FILE_NAME GTH_POTENTIALS
SURFACE_DIPOLE_CORRECTION TRUE
&MGRID
CUTOFF 400
REL_CUTOFF 60
NGRIDS 4
&END MGRID
&QS
EPS_DEFAULT 1.0E-14
MAP_CONSISTENT
&END QS
&SCF
&OT
PRECONDITIONER FULL_SINGLE_INVERSE
MINIMIZER CG
&END OT
SCF_GUESS ATOMIC
EPS_SCF 1.0E-8
MAX_SCF 500
&MIXING
METHOD BROYDEN_MIXING
ALPHA   0.1
BETA    1.5
NBROYDEN 8
&END MIXING
&END SCF
```

```
&XC
&XC_FUNCTIONAL PBE
&PBE
PARAMETRIZATION ORIG
&END PBE
&END XC_FUNCTIONAL
&VDW_POTENTIAL
DISPERSION_FUNCTIONAL PAIR_POTENTIAL
&PAIR_POTENTIAL
TYPE DFTD3
REFERENCE_FUNCTIONAL PBE
CALCULATE_C9_TERM .TRUE.
PARAMETER_FILE_NAME dftd3.dat
R_CUTOFF 15.0
VERBOSE_OUTPUT .TRUE.
&END PAIR_POTENTIAL
&END vdw_POTENTIAL
&END XC
&POISSON
POISSON_SOLVER PERIODIC
&END POISSON
&END DFT
&SUBSYS
&CELL
A   1.1437999725300001E+01    0.0000000000000000E+00    0.0000000000000000E+00
B   0.0000000000000000E+00    8.3859996795999994E+00    0.0000000000000000E+00
C   0.0000000000000000E+00    0.0000000000000000E+00    2.4180000305200000E+01
PERIODIC XYZ
&END CELL
&TOPOLOGY
COORD_FILE_NAME final.xyz
COORDINATE XYZ
&END TOPOLOGY
&KIND Al
ELEMENT   Al
BASIS_SET DZVP-MOLOPT-SR-GTH-q3
POTENTIAL GTH-PBE-q3
&END KIND
&KIND O
ELEMENT   O
BASIS_SET TZVP-MOLOPT-GTH-q6
POTENTIAL GTH-PBE-q6
&END KIND
&KIND C
ELEMENT   C
BASIS_SET TZVP-MOLOPT-GTH-q4
```

```
POTENTIAL GTH-PBE-q4
&END KIND
&KIND H
ELEMENT   H
BASIS_SET TZVP-MOLOPT-GTH-q1
POTENTIAL GTH-PBE-q1
&END KIND
&KIND Mg
ELEMENT   Mg
BASIS_SET DZVP-MOLOPT-SR-GTH-q10
POTENTIAL GTH-PBE-q10
&END KIND
&KIND Cu
ELEMENT   Cu
BASIS_SET DZVP-MOLOPT-SR-GTH-q11
POTENTIAL GTH-PBE-q11
&END KIND
&KIND Ca
ELEMENT   Ca
BASIS_SET DZVP-MOLOPT-SR-GTH-q10
POTENTIAL GTH-PBE-q10
&END KIND
&KIND Au
ELEMENT   Au
BASIS_SET DZVP-MOLOPT-SR-GTH-q11
POTENTIAL GTH-PBE-q11
&END KIND
&KIND Ag
ELEMENT   Ag
BASIS_SET DZVP-MOLOPT-SR-GTH-q11
POTENTIAL GTH-PBE-q11
&END KIND
&KIND Pt
ELEMENT   Pt
BASIS_SET DZVP-MOLOPT-SR-GTH-q18
POTENTIAL GTH-PBE-q18
&END KIND
&KIND Pd
ELEMENT   Pd
BASIS_SET DZVP-MOLOPT-SR-GTH-q18
POTENTIAL GTH-PBE-q18
&END KIND
&KIND Ni
ELEMENT   Ni
BASIS_SET DZVP-MOLOPT-SR-GTH-q18
POTENTIAL GTH-PBE-q18
```

```
&END KIND
&KIND Rh
ELEMENT   Rh
BASIS_SET DZVP-MOLOPT-SR-GTH-q17
POTENTIAL GTH-PBE-q17
&END KIND
&KIND Ir
ELEMENT   Ir
BASIS_SET DZVP-MOLOPT-SR-GTH-q17
POTENTIAL GTH-PBE-q17
&END KIND
&END SUBSYS
&END FORCE_EVAL
&GLOBAL
PROJECT Al2O3_100_term1_Au1_UKS
RUN_TYPE GEO_OPT
PRINT_LEVEL MEDIUM
&END GLOBAL
&MOTION
&CONSTRAINT
&FIXED_ATOMS
LIST=124..161
&END FIXED_ATOMS
&END CONSTRAINT
&GEO_OPT
MAX_FORCE 0.0004
MAX_ITER 2000
OPTIMIZER BFGS
TYPE MINIMIZATION
&END GEO_OPT
&END MOTION
```

A.3 XYZ File (Example Au adsorption on Al_2O_3 (100) site A)

```
161
Au       8.9701037411      5.9671468252     16.2798297944
Al       3.9424856282      4.8191865202      8.0792523196
Al       5.3540395319      0.6212885556      6.1078050331
Al       5.6302595689      0.3919260636     13.8818026428
Al       1.0591483147      0.6530647778      3.1425858944
Al       1.0567240955      0.6182767858     11.0381371353
Al       2.5645764100      4.8220449286      3.1270047187
```

Al	2.4835403666	4.7984500925	11.0007506969
Al	1.0498638799	4.8129464838	8.0751180596
Al	2.5126456740	0.6226261428	6.1049874392
Al	2.5717228539	0.5972702842	13.9713490149
Al	5.3091524180	4.8241428317	5.0994949025
Al	4.9849641323	4.7674701984	13.1736772163
Al	3.9930132401	0.5946190550	9.1109559764
Al	3.8978764555	7.5490205920	4.0356976102
Al	3.8892670375	7.5202971856	11.9789097505
Al	5.3821271263	6.2522299114	10.1905212232
Al	5.3679971183	3.3315880991	10.1765710542
Al	3.9086239503	2.0978588700	4.0376012395
Al	3.8047139318	2.1179173308	11.9698207125
Al	2.4479857368	3.3781969582	6.0038860423
Al	2.1571111289	3.3118237750	13.8074554050
Al	1.1288083167	2.0604483825	8.1875447023
Al	1.1212462433	7.5633355146	8.1869022426
Al	2.4466546198	6.2537410773	6.0038573977
Al	2.0683712255	6.0053643243	13.7954971062
Al	9.6583263128	4.8201598535	8.0803017031
Al	11.0726769314	0.6219865233	6.1075314448
Al	11.3598504897	0.3867954675	13.9137225251
Al	6.7781847595	0.6530572506	3.1425448179
Al	6.7848968035	0.6014142249	11.0239101767
Al	8.2836027900	4.8219128339	3.1268368465
Al	8.1996393406	4.8042756181	11.0078424791
Al	6.7687328756	4.8110701340	8.0765484581
Al	8.2315438613	0.6220538397	6.1057582950
Al	8.2862967397	0.5924166932	13.9689243244
Al	11.0280562948	4.8241447068	5.0994765206
Al	10.7422357297	4.7553199514	13.1390013632
Al	9.7129098916	0.5937532458	9.1108165175
Al	9.6167775259	7.5490578556	4.0356942671
Al	9.6045321295	7.5143487002	11.9839976683
Al	11.1058363414	6.2613656130	10.1854915088
Al	11.0822405583	3.3322375022	10.1681372604
Al	9.6274244385	2.0978064792	4.0375701528
Al	9.5266967633	2.1129960551	11.9755316544
Al	8.1670448447	3.3778813242	6.0038552956
Al	7.8303915735	3.2779079402	13.7906557199
Al	6.8466985307	2.0601537681	8.1873874905
Al	6.8385734232	7.5573988208	8.1865851674
Al	8.1657044290	6.2528869153	6.0033625803
Al	7.7768474142	6.0082921577	13.8330158182
O	1.1122339361	4.8153804206	6.1022452996
O	0.8745247902	4.6650778169	14.0245265567

O	2.4575808226	0.6176229194	8.1293881886
O	5.3148086347	0.6271039452	4.2691367833
O	5.3270428530	0.6164139169	12.1106580181
O	3.9721626975	4.8112750223	9.9256827670
O	3.8334294469	4.8155375491	6.2164238493
O	3.4163046619	4.8125992020	14.1752041099
O	5.4585591373	0.6158125645	7.9770455982
O	2.5752858527	0.6277191863	4.1278085519
O	2.6010380982	0.5554643303	12.0297004981
O	0.9510502670	4.8157933094	10.0694767722
O	1.1832511624	1.9272888059	6.2885339377
O	1.1201056873	1.7183152079	14.2729780864
O	2.3901677352	3.5097390058	7.9063486850
O	2.3903114987	6.1191299628	7.9060056955
O	1.1830911051	7.7012636994	6.2872415183
O	1.3551275489	7.6044437410	14.2643655906
O	5.2416529383	6.2286025548	4.0466100763
O	5.1653476139	6.2005325710	12.0731417906
O	4.0525498847	7.5495172831	10.1531765028
O	4.0444097512	2.0159260043	10.1517855455
O	5.2455211289	3.4179162965	4.0497741685
O	5.0834091681	3.4219851634	12.0028290872
O	3.8155469073	1.9344584579	5.9592387691
O	3.5784820646	2.0921172782	13.8713955990
O	5.4730540713	3.4989643311	8.2355533210
O	5.4715586305	6.1216063524	8.2313244988
O	3.8155998759	7.6980489933	5.9584174859
O	4.0443477545	7.9069234692	14.0175604690
O	2.6086366801	6.2210762894	4.2010918784
O	2.5336378848	6.2200256898	12.0870634923
O	0.9649384476	7.5879111351	9.9953512273
O	0.9612721939	2.0265386175	9.9898874597
O	2.6082641716	3.4154488558	4.1990589774
O	2.3875707971	3.3471347258	12.0069747271
O	6.8313420590	4.8148816322	6.1019818179
O	6.5899769627	4.6587794979	14.0222799324
O	8.1760297331	0.6163158614	8.1307842001
O	11.0337741904	0.6272088063	4.2691261595
O	11.0520534668	0.6153361383	12.1492508841
O	9.6903327797	4.8116946090	9.9269927551
O	9.5529554281	4.8156143704	6.2167181023
O	9.1521837403	4.7487404044	14.1056286238
O	11.1762532199	0.6173397070	7.9754838278
O	8.2941243159	0.6276552470	4.1279174817
O	8.3261031387	0.5540600672	12.0223053043
O	6.6699171609	4.8128814098	10.0702984338

O	6.9020499173	1.9267131881	6.2887341730
O	6.8312371381	1.7171311438	14.2685771463
O	8.1094024580	3.5090161672	7.9062654818
O	8.1098783182	6.1173942290	7.9052973590
O	6.9019911059	7.7004885522	6.2873106263
O	7.0544669570	7.6206845804	14.1905466364
O	10.9606439670	6.2286103777	4.0465704399
O	10.8908427732	6.2017651183	12.0691950417
O	9.7713558157	7.5502401180	10.1564351537
O	9.7647830248	2.0132423757	10.1533926672
O	10.9645829464	3.4178652866	4.0498370222
O	10.8066483422	3.4151827613	11.9922125989
O	9.5342435954	1.9343727470	5.9591522420
O	9.2894909760	2.0866740928	13.8716145542
O	11.1913901926	3.5002561621	8.2344021711
O	11.1918584236	6.1245570187	8.2323516855
O	9.5344354911	7.6979084217	5.9583856631
O	9.7659289872	7.9040444533	14.0199679122
O	8.3277413326	6.2209533591	4.2009085606
O	8.2552319681	6.2161373393	12.1019222775
O	6.6936793793	7.5565405992	9.9964378166
O	6.6809841188	2.0219933495	9.9898577552
O	8.3272411651	3.4154214336	4.1990550889
O	8.1064175839	3.3442215937	12.0034424120
Al	4.0016984924	4.8494558360	0.1881204024
Al	1.1216101616	4.8494558360	0.1910220024
Al	4.0313229574	0.6565399149	1.1792585907
Al	5.4354519867	6.3262305222	2.2424531074
Al	5.4354519867	3.3726811415	2.2424531074
Al	1.1778852918	2.0939841284	0.2744430035
Al	1.1778852918	7.6050114624	0.2744430035
Al	9.7206983550	4.8494558360	0.1881204024
Al	6.8406100242	4.8494558360	0.1910220024
Al	9.7503233005	0.6565399149	1.1792585907
Al	11.1544513690	6.3262305222	2.2424531074
Al	11.1544513690	3.3726811415	2.2424531074
Al	6.8968853946	2.0939841284	0.2744430035
Al	6.8968853946	7.6050114624	0.2744430035
O	2.5098402454	0.6565399149	0.1958580025
O	4.0199995093	4.8494558360	2.0059728737
O	5.4763998999	0.6565399149	0.0309504004
O	1.0554986032	4.8494558360	2.1604831240
O	2.4477319755	3.5443427562	0.0000000000
O	2.4477319755	6.1544852236	0.0000000000
O	4.0872550048	7.6360397366	2.2351992040
O	4.0872550048	2.0629560973	2.2351992040

```
O       5.5334754042      3.5420784944      0.3508518044
O       5.5334754042      6.1567497286      0.3508518044
O       0.9989948846      7.6460189840      2.0710170261
O       0.9989948846      2.0529766067      2.0710170261
O       8.2288408287      0.6565399149      0.1958580025
O       9.7389993719      4.8494558360      2.0059728737
O      11.1953992822      0.6565399149      0.0309504004
O       6.7744979855      4.8494558360      2.1604831240
O       8.1667318382      3.5443427562      0.0000000000
O       8.1667318382      6.1544852236      0.0000000000
O       9.8062543871      7.6360397366      2.2351992040
O       9.8062543871      2.0629560973      2.2351992040
O      11.2524757358      3.5420784944      0.3508518044
O      11.2524757358      6.1567497286      0.3508518044
O       6.7179946900      7.6460189840      2.0710170261
O       6.7179946900      2.0529766067      2.0710170261
```

A.4 Input File (Example HOMO-LUMO gap of gas phase Au)

```
&FORCE_EVAL
METHOD QS
&DFT
UKS  T
RELAX_MULTIPLICITY     1.0000000000000000E-02
BASIS_SET_FILE_NAME BASIS_MOLOPT
POTENTIAL_FILE_NAME GTH_POTENTIALS
SURFACE_DIPOLE_CORRECTION TRUE
&MGRID
CUTOFF 400
REL_CUTOFF 60
NGRIDS 4
&END MGRID
&QS
EPS_DEFAULT 1.0E-14
MAP_CONSISTENT
&END QS
&SCF
&OT
PRECONDITIONER FULL_SINGLE_INVERSE
MINIMIZER CG
&END OT
SCF_GUESS ATOMIC
EPS_SCF 1.0E-8
```

```
MAX_SCF 500
&MIXING
METHOD BROYDEN_MIXING
ALPHA   0.1
BETA    1.5
NBROYDEN  8
&END MIXING
&END SCF
&XC
&XC_FUNCTIONAL PBE
&PBE
PARAMETRIZATION ORIG
&END PBE
&END XC_FUNCTIONAL
&VDW_POTENTIAL
DISPERSION_FUNCTIONAL PAIR_POTENTIAL
&PAIR_POTENTIAL
TYPE DFTD3
REFERENCE_FUNCTIONAL PBE
CALCULATE_C9_TERM .TRUE.
PARAMETER_FILE_NAME dftd3.dat
R_CUTOFF 15.0
VERBOSE_OUTPUT .TRUE.
&END PAIR_POTENTIAL
&END vdw_POTENTIAL
&END XC
&POISSON
POISSON_SOLVER PERIODIC
&END POISSON
&PRINT
&E_DENSITY_CUBE
&END E_DENSITY_CUBE
&MO
EIGENVALUES        .TRUE.
OCCUPATION_NUMBERS .TRUE.
EIGENVECTORS       .FALSE.
&END MO
&MO_CUBES
WRITE_CUBE F
NHOMO 20
NLUMO 20
&END MO_CUBES
&END PRINT
&END DFT
&SUBSYS
&CELL
```

```
A  10.0000000000        0.0000000000        0.0000000000
B   0.0000000000       10.0000000000        0.0000000000
C   0.0000000000        0.0000000000       10.0000000000
PERIODIC XYZ
&END CELL
&TOPOLOGY
COORD_FILE_NAME final.xyz
COORDINATE XYZ
&END TOPOLOGY
&KIND Al
ELEMENT   Al
BASIS_SET DZVP-MOLOPT-SR-GTH-q3
POTENTIAL GTH-PBE-q3
&END KIND
&KIND O
ELEMENT   O
BASIS_SET TZVP-MOLOPT-GTH-q6
POTENTIAL GTH-PBE-q6
&END KIND
&KIND C
ELEMENT   C
BASIS_SET TZVP-MOLOPT-GTH-q4
POTENTIAL GTH-PBE-q4
&END KIND
&KIND H
ELEMENT   H
BASIS_SET TZVP-MOLOPT-GTH-q1
POTENTIAL GTH-PBE-q1
&END KIND
&KIND Mg
ELEMENT   Mg
BASIS_SET DZVP-MOLOPT-SR-GTH-q10
POTENTIAL GTH-PBE-q10
&END KIND
&KIND Cu
ELEMENT   Cu
BASIS_SET DZVP-MOLOPT-SR-GTH-q11
POTENTIAL GTH-PBE-q11
&END KIND
&KIND Ca
ELEMENT   Ca
BASIS_SET DZVP-MOLOPT-SR-GTH-q10
POTENTIAL GTH-PBE-q10
&END KIND
&KIND Au
ELEMENT   Au
```

```
BASIS_SET DZVP-MOLOPT-SR-GTH-q11
POTENTIAL GTH-PBE-q11
&END KIND
&KIND Ag
ELEMENT   Ag
BASIS_SET DZVP-MOLOPT-SR-GTH-q11
POTENTIAL GTH-PBE-q11
&END KIND
&KIND Pt
ELEMENT   Pt
BASIS_SET DZVP-MOLOPT-SR-GTH-q18
POTENTIAL GTH-PBE-q18
&END KIND
&KIND Pd
ELEMENT   Pd
BASIS_SET DZVP-MOLOPT-SR-GTH-q18
POTENTIAL GTH-PBE-q18
&END KIND
&KIND Ni
ELEMENT   Ni
BASIS_SET DZVP-MOLOPT-SR-GTH-q18
POTENTIAL GTH-PBE-q18
&END KIND
&KIND Rh
ELEMENT   Rh
BASIS_SET DZVP-MOLOPT-SR-GTH-q17
POTENTIAL GTH-PBE-q17
&END KIND
&KIND Ir
ELEMENT   Ir
BASIS_SET DZVP-MOLOPT-SR-GTH-q17
POTENTIAL GTH-PBE-q17
&END KIND
&END SUBSYS
&END FORCE_EVAL
&GLOBAL
PROJECT Au
RUN_TYPE GEO_OPT
PRINT_LEVEL MEDIUM
&END GLOBAL
&MOTION
&GEO_OPT
MAX_FORCE 0.0004
MAX_ITER 2000
OPTIMIZER BFGS
TYPE MINIMIZATION
```

```
&END GEO_OPT
&END MOTION
```

Appendix B Supporting Figures

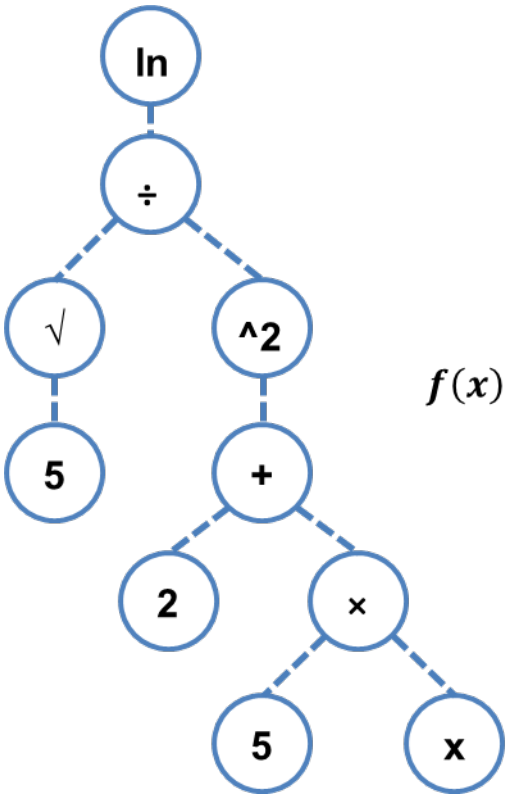

$$f(x) = ln(\frac{(5x+2)^2}{\sqrt{5}})$$

Figure S1 An equation generated randomly by symbolic regression.

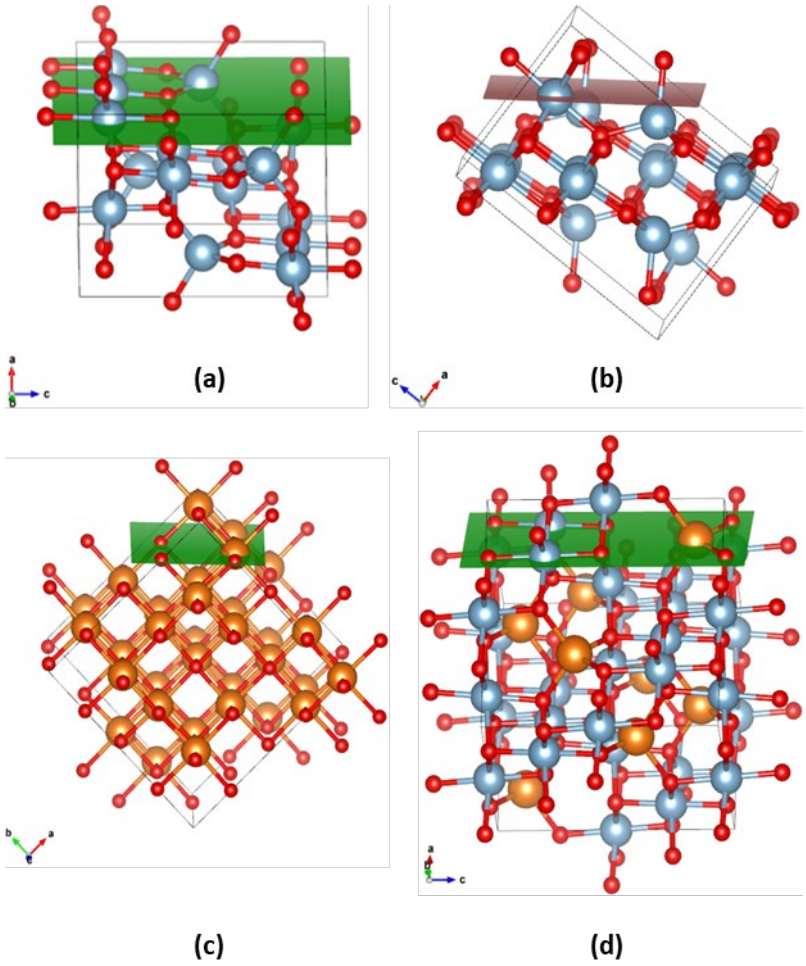

Figure S2 Structures of surface facets which are not the most stable ones: (a) γ-Al_2O_3 (110), (b) γ-Al_2O_3 (111), (c) MgO (110), and (d) $MgAl_2O_4$ (110). The surface cleaving plane is highlighted in green and brown. Orange atoms represent Mg, grey atoms represent Al, and red atoms represent O.

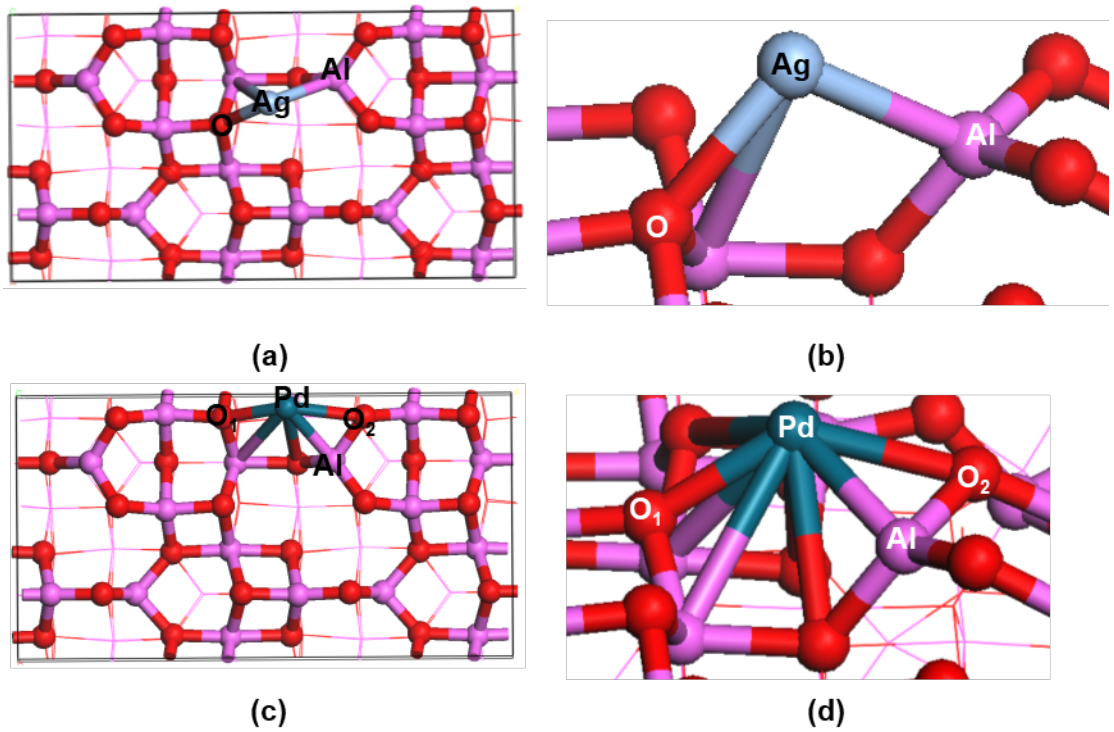

Figure S3 Ag adsorption on γ-Al_2O_3 (110) in (a) top view, (b) side view; Pd adsorption on γ-Al_2O_3 (110) in (a) top view, (b) side view. Grey atoms represent Ag, blue atoms represent Pd, pink atoms represent Al, and red atoms represent O.

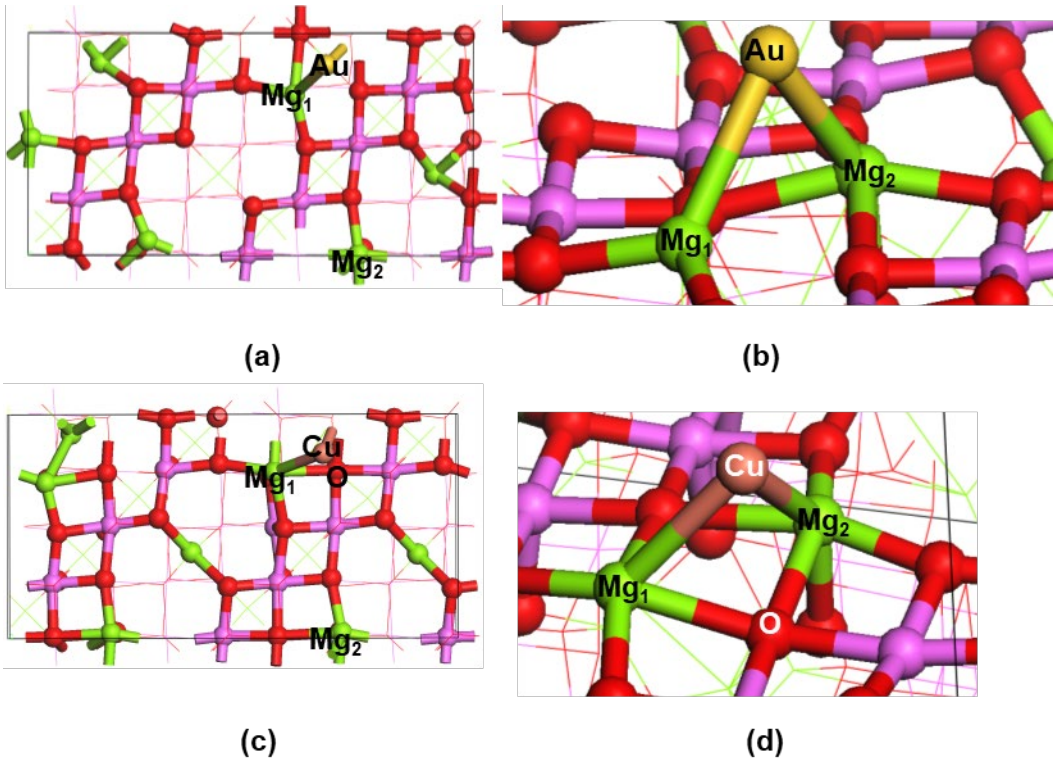

Figure S4 Au adsorption on $MgAl_2O_4$ (100) in (a) top view, (b) side view; Cu adsorption on $MgAl_2O_4$ (100) in (c) top view, (d) side view. Yellow atoms represent Au, copper atoms represent Cu, green atoms represent Mg, pink atoms represent Al, and red atoms represent O.

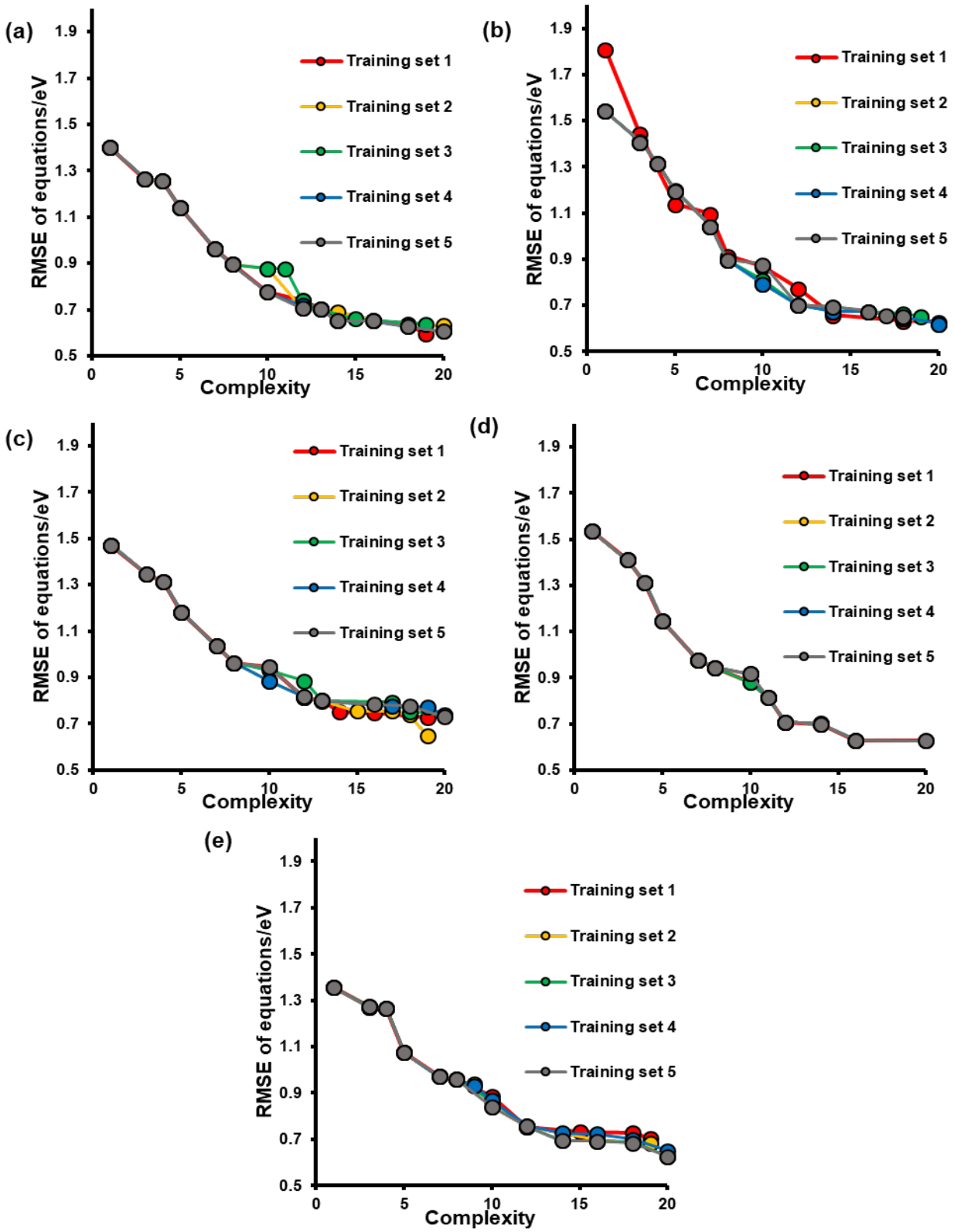

Figure S5 RMSE versus complexity of equations generated in Eureqa by training data of (a) dataset 1, (b) dataset 2, (c) dataset 3, (d) dataset 4, and (e) dataset 5.

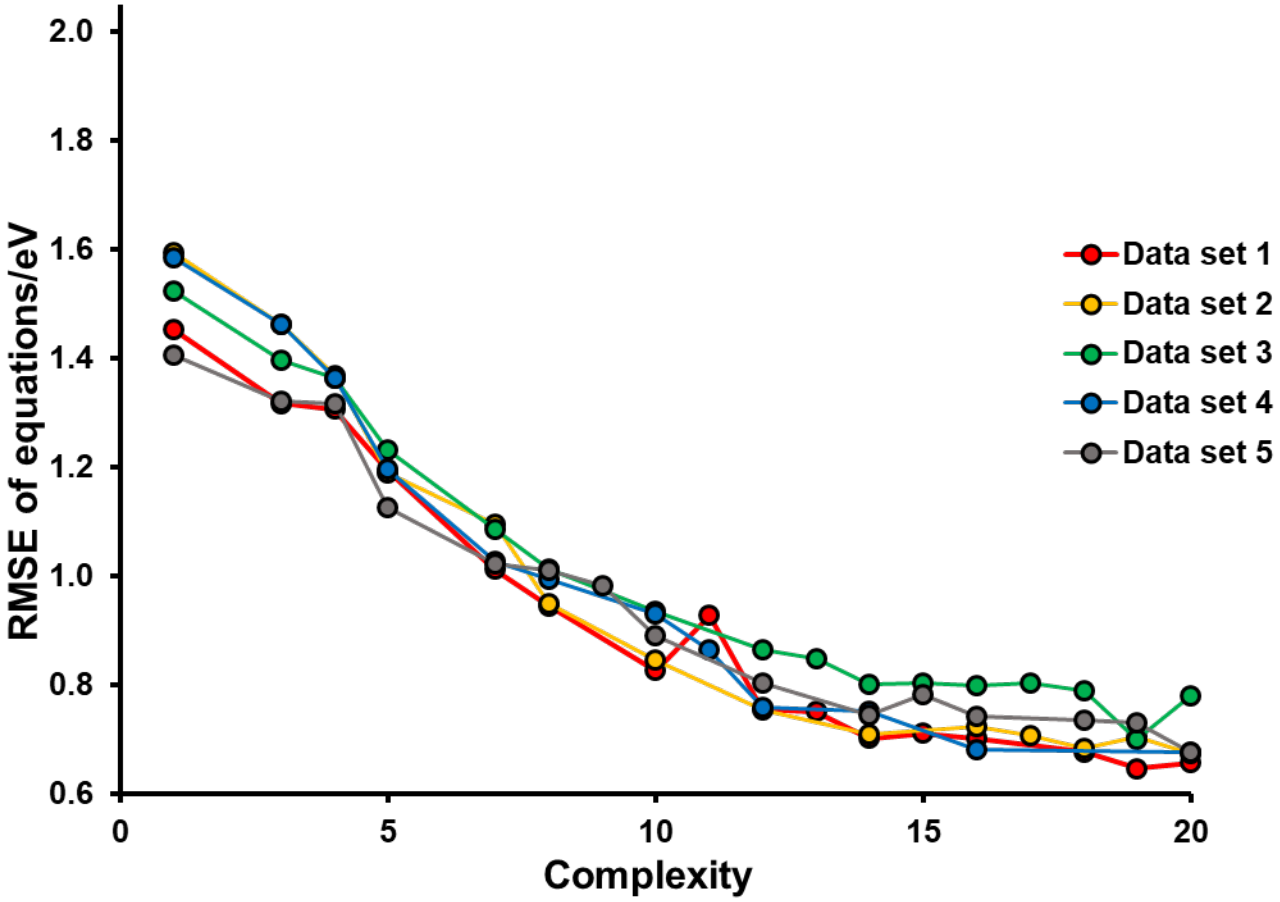

Figure S6 Pareto Front plotted by using the lowest RMSE error in each dataset for a particular complexity.

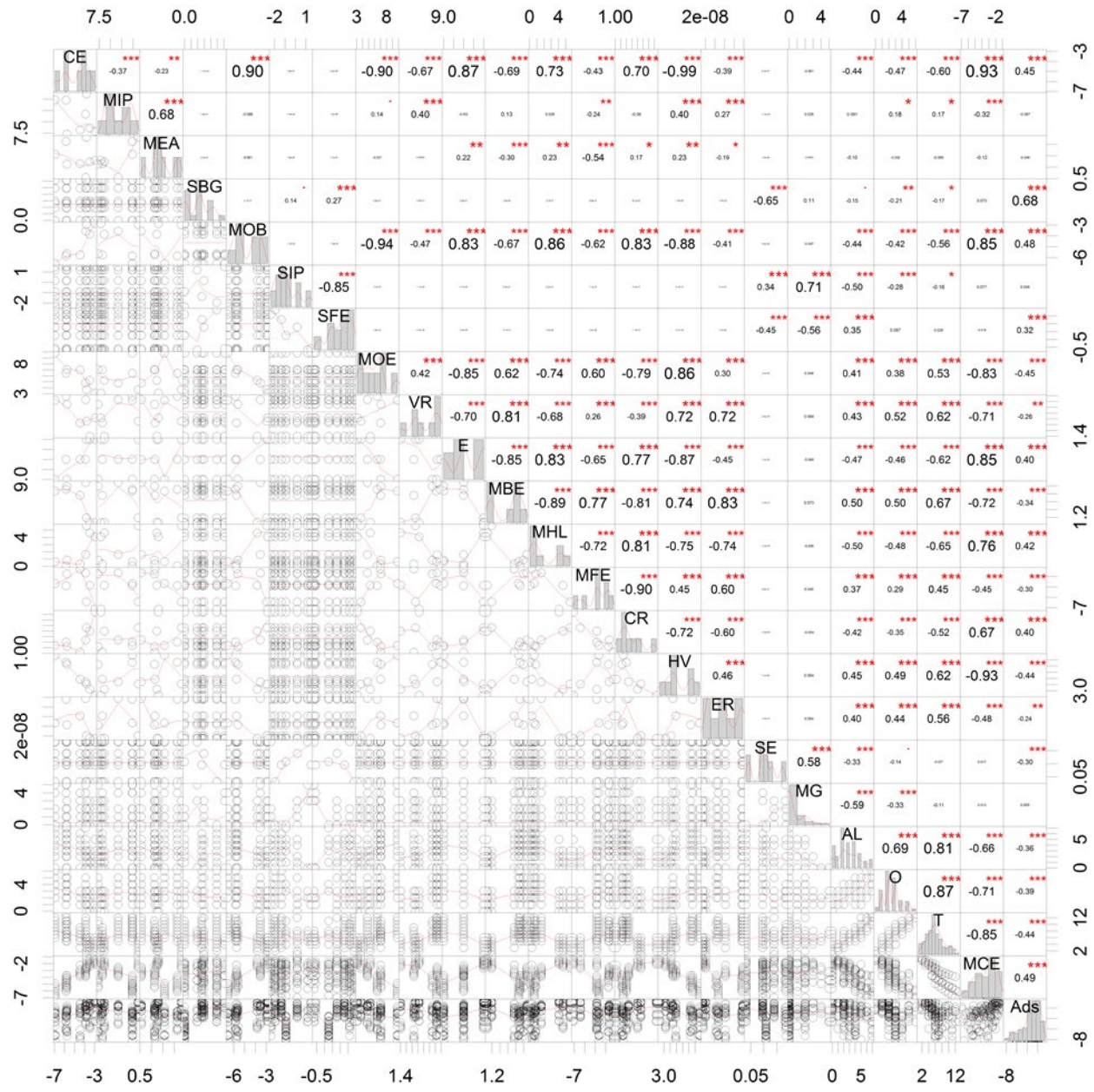

Figure S7 Correlation Matrix of physical properties indicated by Eureqa. Along the diagonal are histograms of the selected descriptors. Correlation coefficients between the different descriptors are plotted in the upper right triangle, with a font chosen to convey their magnitude (e.g. the best correlations are the largest, near-zero correlations are written with a tiny font). Plots of the two descriptors versus one another are in the lower left triangle. As an example, the correlation coefficient between MOB and MOE is -0.94, and their plot can be found on the leftmost column, three squares up from the bottom.

Appendix C Supporting Tables

Table S1 Cell configurations, layers, and lattice constants used in optimizing the surface facets.

Surface facet	Clean cell	Layers	Lattice constant/ Å		
			a	b	c
γ-Al_2O_3 (100)	$Al_{64}O_{96}$	14	11.438	8.386	24.180
γ-Al_2O_3 (110)	$Al_{64}O_{96}$	8	8.386	15.795	20.256
γ-Al_2O_3 (111)	$Al_{64}O_{96}$	12	9.798	16.772	18.638
MgO (100)	$Mg_{32}O_{32}$	4	8.748	8.717	21.647
MgO (110)	$Mg_{32}O_{32}$	4	8.717	12.362	19.759
$MgAl_2O_4$ (100)	$Mg_{16}Al_{32}O_{64}$	8	16.424	8.212	17.300
$MgAl_2O_4$ (110)	$Mg_{16}Al_{32}O_{64}$	8	8.212	11.614	20.323

Table S2 Valence electron configurations of supported metals[74].

Metal	Valence configuration
Au	$[Xe]4f^{14}5d^{10}6s$
Cu	$[Ar]3d^{10}4s$
Ag	$[Kr]4d^{10}5s$
Pt	$[Xe]4f^{14}5d^{9}6s$
Pd	$[Kr]4d^{10}$
Ni	$[Ar]3d^{8}4s^{2}$
Rh	$[Kr]4d^{8}5s$
Ir	$[Xe]4f^{14}5d^{7}6s^{2}$

Table S3a Physical properties of supported metal from literature.

Metal	Experimental bulk cohesive energy of supported metal/eV[73]	Experimental ionization potential of supported metal/eV[74]	Experimental electron affinity of supported metal/eV[74]	Oxidation enthalpy of supported metal/eV[19]	Van del Waal radius of supported metal/Å[75-76]
Au	-3.81	9.2255	2.30863	3.7116	1.66
Cu	-3.49	7.7264	1.235	5.2522	1.4
Ag	-2.95	7.5762	1.302	3.1113	1.72
Pt	-5.84	8.9588	2.128	6.4227	2.09
Pd	-3.89	8.3369	0.562	4.792	2.03
Ni	-4.44	7.6398	1.156	7.003	1.63
Rh	-5.75	7.4589	1.137	7.063	1.95
Ir	-6.94	8.967	1.5638	9.8041	2.02

Table S3b Physical properties of supported metal from literature (continued).

Metal	Electron configuration of supported metal/(e/atom)[74]	Martynov–Batsanov electronegativity of supported metal[19]	Covalent radius of triple bond of supported metal/Å[77]	Heat of vaporization of supported metal/(eV/atom)[78]	Electronical resistivity of supported metal (273K)/Ω*m[74]
Au	11	1.19	1.23	3.5568	2.05E-08
Cu	11	1.08	1.2	3.12416	1.54E-08
Ag	11	1.07	1.37	2.6416	1.47E-08
Pt	10	1.91	1.1	5.304	9.60E-08
Pd	10	2.08	1.12	3.7232	9.78E-08
Ni	10	1.76	1.01	3.9416	6.16E-08
Rh	9	1.99	1.06	5.1376	4.30E-08
Ir	9	1.87	1.07	5.8656	4.70E-08

Table S3c The metal-oxygen binding energy of supported metal calculated by CP2K program package[46].

Metal	E_M/eV	E_O/eV	E_{M+O}/eV	E_{M-O}/eV	Spin-state of the metal-oxygen complex
Au	-901.8916943	-430.9313623	-1335.787958	-2.964901042	0
Cu	-1306.121609		-1740.886622	-3.833651054	0
Ag	-1005.078453		-1438.869247	-2.859431633	0
Pt	-3264.330644		-3701.097346	-5.835339304	3
Pd	-3459.111873		-3893.593769	-3.550533389	3
Ni	-4601.989526		-5038.670081	-5.749192419	3
Rh	-2997.570383		-3434.134719	-5.632973714	4
Ir	-2862.277935		-3299.759153	-6.549855499	4

E_M is energy of gas phase supported metal atom

E_O is energy of gas phase oxygen atom

E_{M+O} is energy of supported metal atom coordinate with oxygen

E_{M-O} is metal-oxygen binding energy of supported metal atom

Table S3d Physical properties of supported metal calculated by CP2K program package[46].

Metal	HOMO-LUMO gap of supported metal/eV	Fermi energy of supported metal/eV
Au	5.599745	-6.419821
Cu	4.621396	-4.839916
Ag	4.084015	-7.102894
Pt	0.065967	-4.866576
Pd	1.620239	-3.663211
Ni	0.315045	-3.279004
Rh	0.853019	-3.74123
Ir	0.636881	-4.657139

Table S3e Ionization potential of oxide support calculated by CP2K program package[46].

Surface facet	E ($Slab^+$)/a.u.	E (Slab)/a.u.	IP_s/eV
γ-Al_2O_3 (100)	-1682.657456	-1682.585509	-1.957754172
γ-Al_2O_3 (100)	-1681.948752	-1681.898416	-1.369709954
γ-Al_2O_3 (100)	-1681.567472	-1681.533834	-0.915306751
MgO (100)	-2542.204887	-2542.259826	1.49493741
MgO (110)	-2541.336647	-2541.380045	1.180909141
$MgAl_2O_4$ (100)	-2112.106077	-2112.11214	0.164967487
$MgAl_2O_4$ (110)	-2112.283381	-2112.196836	-2.354990392

$$IP_s = E\ (Slab^+) - E\ (Slab)$$

IP_s is ionization potential of oxide support, E ($Slab^+$) is the energy of surface slab cation, and E (Slab) is the energy of surface slab.

Table S3f Physical properties of oxide support calculated by CP2K program package[46].

Surface facet	Band gap of oxide support/eV	Fermi energy of oxide support/eV	Calculated surface energy of oxide support/eV/Å^2
γ-Al_2O_3 (100)	2.449223	1.884327	0.031522388
γ-Al_2O_3 (100)	1.312146	1.268465	0.095494626
γ-Al_2O_3 (100)	0	0.268132	0.108051033
MgO (100)	3.049584	-0.573668	0.095568656
MgO (110)	0.957561	-0.665112	0.181995043
$MgAl_2O_4$ (100)	1.468544	0.789313	0.139333601
$MgAl_2O_4$ (110)	0.000235	1.597015	0.184607

Table S4 The information of most preferred sites of supported metals on different surface facets (Unit for distances is Å).

γ-Al_2O_3 (100), supported metal in hollow site between two oxygens

Metal	M-O_1 distance	M-O_2 distance	Average M-O distance	Adsorption energy/eV
Au	2.644	2.286	2.465	-0.971765179
Cu	2.068	1.959	2.0135	-1.638644248
Ag	2.543	2.646	2.5945	-0.794451679
Pt	2.078	2.038	2.058	-4.62211681
Pd	1.976	2.355	2.1655	-2.585990582
Ni	1.977	1.907	1.942	-3.553911313
Rh	1.991	2.346	2.1685	-3.566181225
Ir	2.055	2.005	2.03	-4.560746808

γ-Al_2O_3 (110), supported metal in hollow site between Al and O

Metal	M-Al distance	M-O distance	Average M-Al, M-O distance	Adsorption energy/eV
Au	2.546	2.357	2.4515	-1.488570299
Cu	2.545	1.985	2.265	-1.635164761
Ag	2.636	2.359	2.4975	-1.180406717

γ-Al_2O_3 (110), supported metal in hollow site

Metal	M-O_1 distance	M-O_2 distance	Average M-O distance	Adsorption energy/eV
Pt	2.041	2.032	2.0365	-3.711390283
Pd	2.368	2.560	2.464	-2.199992913
Ni	1.882	1.819	1.8505	-3.135086839
Rh	2.053	1.983	2.018	-2.681001727
Ir	2.014	1.964	1.989	-3.873928904

Table S4 The information of most preferred sites of supported metals on different surface facets (Unit for distances is Å) (continued).

γ-Al_2O_3 (111), supported metal in hollow site

Metal	M-O_1 distance	M-O_2 distance	M-O_3 distance	Average M-O distance	Adsorption energy/eV
Au	2.202	2.182	2.522	2.302	-3.753245262
Cu	2.01	1.973	1.873	1.952	-5.962277018
Ag	2.287	2.31	2.394	2.330333333	-4.543309413
Pt	2.093	1.802	2.219	1.798	-6.348793035
Pd	2.14	2.139	2.105	2.128	-5.134024784
Ni	1.965	1.935	1.909	1.936333333	-8.043296895
Rh	1.961	1.949	1.962	1.957333333	-7.362943959
Ir	1.945	1.928	1.936	1.936333333	-8.24674053

MgO (100), supported metal on top oxygen site

Metal	M-O distance	Adsorption energy/eV
Au	2.281	-1.083705048
Cu	1.945	-0.976707065
Ag	2.342	-0.684878487
Pt	1.96	-3.06922768
Pd	2.061	-1.675659784
Ni	1.805	-1.98155824

MgO (100), supported metal in hollow site

Metal	M-O_1 distance	M-O_2 distance	Average M-O distance	Adsorption energy/eV
Rh	2.472	2.139	2.3055	-2.033494128
Ir	2.857	1.997	2.427	-2.563721377

Table S4 The information of most preferred sites of supported metals on different surface facets (Unit for distances is Å) (continued).

MgO (110), supported metal in a hollow site between two oxygens

Metal	$M\text{-}O_1$ distance	$M\text{-}O_2$ distance	Average M-O distance	Adsorption energy/eV
Au	2.412	2.445	2.4285	-2.096405264
Cu	1.967	1.993	1.98	-2.56815116
Ag	2.288	2.347	2.3175	-2.082625102
Pd	2.098	2.45	2.274	-2.54276557
Ni	1.827	1.975	1.901	-3.838469141
Rh	2.031	2.191	2.111	-3.77759117
Ir	1.972	2.215	2.0935	-4.725384325

MgO (110), supported metal on top of oxygen site

Metal	M-O distance	Adsorption energy/eV
Pt	1.948	-4.481155234

$MgAl_2O_4$ (100), supported metal on Mg bridge site

Metal	$M\text{-}Mg_1$ distance	$M\text{-}Mg_2$ distance	Average M-Mg distance	Adsorption energy/eV
Au	2.773	2.851	2.812	-2.379317883
Cu	2.771	2.856	2.8135	-1.814059648
Ag	3.265	2.851	3.058	-1.206393017

$MgAl_2O_4$ (100), supported metal in hollow site

Metal	M-O distance	Adsorption energy/eV
Pt	1.996	-3.88688492
Pd	2.085	-1.806300157
Ni	1.778	-2.948917747

Table S4 The information of most preferred sites of supported metals on different surface facets (Unit for distances is Å) (continued).

$MgAl_2O_4$ (100), supported metal in the hollow site between two oxygens

Metal	M-O_1 distance	M-O_2 distance	Average M-O distance	Adsorption energy/eV
Rh	2.066	2.025	2.0455	-2.755037312
Ir	1.939	2.028	1.9835	-3.612465149

$MgAl_2O_4$ (110), supported metal in the hollow site between two oxygens

Metal	M-O_1 distance	M-O_2 distance	Average M-O distance	Adsorption energy/eV
Au	2.05	2.047	2.0485	-3.238426545
Cu	1.806	1.832	1.819	-4.781967961
Ag	2.192	2.181	2.1865	-3.250601477
Pt	1.907	1.928	1.9175	-5.769915921
Pd	2.065	1.815	1.94	-3.735368639
Ni	1.766	1.759	1.7625	-6.183494928
Rh	1.905	1.921	1.913	-5.496512462
Ir	1.812	1.81	1.811	-7.34314605

Table S5 The standard of counting supported metal coordination numbers.

If the distance between adsorbed metal and atom in the surface is smaller than their coordination distance (d_{CN}), then we consider they coordinate with each other.

For metal-metal binding, d_{CN} is the sum of their Van del Waal radius.

For metal-oxygen binding, d_{CN} is the sum of metal Van der Waal radius and oxygen ionic radius (1.26 Å)[80].

The transition metal Van del Waal radius are listed in Supplementary Table 3a.

Van del Waal radius for Mg[75] and Al[76] are 1.73 Å and 1.84 Å.

Bond	d_{CN}/ Å
Au-Mg	3.39
Au-Al	3.5
Au-O	2.92
Cu-Mg	3.13
Cu-Al	3.24
Cu-O	2.66
Ag-Mg	3.45
Ag-Al	3.56
Ag-O	2.98
Pt-Mg	3.82
Pt-Al	3.93
Pt-O	3.35
Pd-Mg	3.75
Pd-Al	3.86
Pd-O	3.28
Ni-Mg	3.36
Ni-Al	3.47
Ni-O	2.89
Rh-Mg	3.68
Rh-Al	3.79
Rh-O	3.21

Table S5 The standard of counting supported metal coordination numbers (continued).

Bond	d_{CN}/ Å
Ir-Mg	3.75
Ir-Al	3.86
Ir-O	3.28

Table S6 Bootstrapping results for model construction.

Bootstrap sampling uses 10,000 replicates.

Group 1

Complexity	Equation	RMSE (eV)
5	$F(x) = a * SBG + b$	1.381664
9	$F(x) = a * SBG + b * MOB + c$	1.0391853
9	$F(x) = a * SBG + b * MOE + c$	1.0854364
13	$F(x) = a * SE + b * SBG + c * MOB + d$	0.9766593
13	$F(x) = a * SFE + b * SIP + c * MOB + d$	0.9809163
17	$F(x) = a * SE + b * SBG + c * MOB + d * Mg + e$	0.8355649
13	$F(x) = a * SE + b * SBG + c * MOB + d$	0.9766593
17	$F(x) = a * SE + b * SBG + c * MOB + d * Mg + e$	0.7798851
17	$F(x) = a * SFE + b * SIP + c * MOB + d * SBG + e$	0.8818448
21	$F(x) = a * SE + b * SBG + c * MOB + d * MEA + e * Mg + f$	1.01063069
27	$F(x) = a * SE + b * SBG + c * MOB + d * Mg * t + e * t + f * Mg + g$	1.04314050
27	$F(x) = a * SE + b * SBG + c * MOB + d * SE * t + e * t + f * Mg + g$	1.06581488

Table S6 Bootstrapping results for model construction (continued).

Group 2

Complexity	Equation	RMSE (eV)
10	$F(x) = \frac{1}{a * SE + b} + c$	1.7912391
10	$F(x) = \frac{1}{a * SIP + b} + c$	1.885260
14	$F(x) = a * MOB + \frac{1}{b * SBG + c} + d$	1.23097388
14	$F(x) = a * MOB + \frac{1}{b * SE + c} + d$	1.5425028
14	$F(x) = a * MOB + \frac{1}{b * SIP + c} + d$	0.9593233
18	$F(x) = a * SBG + b * MOB + \frac{1}{c * SE + d} + e$	1.0388658
18	$F(x) = a * SBG + b * MOB + \frac{1}{c * SIP + d} + e$	1.0274604
14	$F(x) = a * MOB + \frac{b}{c * SE + d} + e$	1.5425106
14	$F(x) = a * MOB + \frac{b}{c * SIP + d} + e$	0.94622471
14	$F(x) = a * MOB + \frac{b}{c * SBG + d} + e$	0.8049614
18	$F(x) = a * MOB + \frac{b * Mg + c}{d * SIP + e} + f$	0.9383880
18	$F(x) = a * SBG + b * MOB + \frac{c}{d * SE + e} + f$	1.03918289
18	$F(x) = a * SBG + b * MOB + \frac{c}{d * SIP + e} + f$	0.76418773
22	$F(x) = a * SFE + b * SIP + c * MOB + \frac{1}{d * SE + e} + f$	1.0150411
22	$F(x) = a * SFE + b * SIP + c * MOB + \frac{1}{d * SIP + e} + f$	1.0169585

Table S6 Bootstrapping results for model construction (continued).

Group 2

Complexity	Equation	RMSE (eV)
22	$F(x) = a * SFE + b * SIP + c * MOB + \frac{d}{e * SE + f} + g$	0.9600233
22	$F(x) = a * SFE + b * SIP + c * MOB + \frac{d}{e * SFE + f} + g$	0.980916726
26	$F(x) = a * SE + b * SBG + c * MOB + \frac{1}{d * SBG + e} + f * Mg + g$	1.06159545
26	$F(x) = a * SE + b * SBG + c * MOB + \frac{1}{d * SFE + e} + f * Mg + g$	1.02405304
27	$F(x) = a * SBG + b * MOB + \frac{1}{c * SBG + d} + \frac{e}{f * SIP + g} + h$	1.0414007
32	$F(x) = a * SBG + b * MOB + c * SE * t + \frac{1}{d * SE + e} + f * t + g * SE + h$	0.9542535

Table S6 Bootstrapping results for model construction (continued).

Group 3

Complexity	Equation	RMSE (eV)
24	$F(x) = a * MOB + \frac{1}{b * SIP + c} + \frac{d}{\exp(e * SBG)} + f$	0.9167515
24	$F(x) = a * SBG + b * MOB + \frac{1}{c * SE + d} + e * SBG^2 + f$	0.7786195
22	$F(x) = a * MOB + b * SBG + \frac{c * Mg + d}{e * SIP + f} + g$	0.78136774
22	$F(x) = a * SBG + b * MOB + \frac{c * MIP + d}{e * SE + f} + g$	1.0372081
22	$F(x) = a * SBG + b * MOB + \frac{c * MIP + d}{e * SIP + f} + g$	1.0350657
26	$F(x) = a * SE + b * SBG + c * MOB + \frac{1}{d * SBG + e} + f * Mg + g$	1.03419145
26	$F(x) = a * SFE + b * SIP + c * MOB + \frac{1}{d * SIP + e} + f * SE + g$	1.3885672
28	$F(x) = a * MOB + b * SBG * SE + \frac{1}{c * SIP + d} + e * SBG + f * SE + g$	0.7930596
23	$F(x) = a * MOB + \frac{1}{b * SIP + e} + f * \exp(g * SBG) + h$	0.9196913
27	$F(x) = a * SBG + b * MOB + \frac{c}{d * SBG + e} + \frac{f}{g * SIP + h} + i$	1.05017888

Table S6 Bootstrapping results for model construction (continued).

Group 4

Complexity	Equation	RMSE (eV)
18	$F(x) = a * MOB + \frac{b * SIP + c}{d * SBG + e} + f$	0.8471124
18	$F(x) = a * MOB + \frac{b * SFE + c}{d * SBG + e} + f$	0.7669234
22	$F(x) = a * MOB + b * SBG + \frac{c * MIP + d}{e * SE + f} + g$	0.98387606
22	$F(x) = a * MOB + b * SBG + \frac{c * Mg + d}{e * SIP + f} + g * Mg$	0.79288477
22	$F(x) = a * SBG + b * MOB + \frac{c * MIP + d}{e * SIP + f} + g$	0.851006276

Group 5

Complexity	Equation	RMSE (eV)
14	$F(x) = \frac{a * MOE + b}{c * SBG + d} + e$	0.8796041
23	$F(x) = \frac{1}{a * SIP + b} + \frac{c * MOB + d}{e * SBG + f} + g$	0.8580128
23	$F(x) = a * MOB + \frac{b}{c * SIP + d} + \frac{e}{f * SBG + g} + h$	0.754600390

Group 6

Complexity	Equation	RMSE (eV)
14	$F(x) = \frac{a * MOB + b}{c * SBG + d} + e$	0.83760501
16	$F(x) = \frac{a * SBG + b * MOB + c}{d * SBG + e} + f$	0.8376051
26	$F(x) = a * SE * Al + \frac{b * MOB + c}{d * SBG + e} + f * Al + g * SE + h$	0.8257579

Table S6 Bootstrapping results for model construction (continued).

Group 7

Complexity	Equation	RMSE (eV)
17	$F(x) = a * MOB + b * log(c * SBG + d) + e$	0.81590424
21	$F(x) = a * MOB + b * \log(c * SBG + d) + e * Mg + f$	0.7304002
26	$F(x) = a * MOB + \frac{1}{b * SIP + c} + d * log(e * SBG + f) + g$	0.85372357

Group 8

Complexity	Equation	RMSE (eV)
28	$F(x) = a * SBG + b * MOB + \frac{c}{d * SE * Mg + e * Mg + f * SE + g} + h$	0.9770267
32	$F(x) = a * SBG + b * MOB + \frac{1}{c * SE * Mg + d * Mg + e * SE + f} + g * ER + h$	1.0367179
32	$F(x) = a * SBG + b * MOB + c * SIP + \frac{1}{d * SE * Mg + e * Mg + f * SE + g} + h$	1.0360931

Table S6 Bootstrapping results for model construction (continued).

Group 9

Complexity	Equation	RMSE (eV)
22	$F(x) = a * MOB + \frac{b * MOB + * SIP + d}{e * SBG + f} + g$	0.6904047
35	$F(x) = \frac{1}{a * SIP + b} + \frac{b * MOB + c * SE * Al + d * SE + e * Al}{f * SBG + g} + h$	0.81492294
28	$F(x) = a * MOB + \frac{b * MOB + c * MOB * SIP + d * SIP + e}{f * SBG + g} + h$	0.72221069

Group 10

Complexity	Equation	RMSE (eV)
26	$F(x) = a * MOB + b * SBG + \frac{c * Mg + d * MIP + e}{f * SIP + g} + h$	0.989581711
31	$F(x) = a * MOB + \frac{1}{b * Mg + c} + \frac{d * Mg + e}{f * SIP + g} + h * SE + i$	0.788503679
36	$F(x) = a * SBG + b * MOB + c * SE * Al + \frac{d * Mg + e}{f * SIP + g} + h * Al + i * SE + j$	0.80613299

Bibliography

1. Wang, A.; Li, J.; Zhang, T., Heterogeneous Single-Atom Catalysis. *Nature Reviews Chemistry* **2018**, *2*, 65-81.

2. Liu, J.; Bunes, B. R.; Zang, L.; Wang, C., Supported Single-Atom Catalysts: Synthesis, Characterization, Properties, and Applications. *Environmental Chemistry Letters* **2018**, *16*, 477-505.

3. Liu, J., Catalysis by Supported Single Metal Atoms. *ACS Catalysis* **2017**, *7*, 34-59.

4. Yang, X.-F.; Wang, A.; Qiao, B.; Li, J.; Liu, J.; Zhang, T., Single-Atom Catalysts: A New Frontier in Heterogeneous Catalysis. *Accounts of Chemical Research* **2013**, *46*, 1740-1748.

5. Flytzani-Stephanopoulos, M., Gold Atoms Stabilized on Various Supports Catalyze the Water–Gas Shift Reaction. *Accounts of Chemical Research* **2014**, *47*, 783-792.

6. DeRita, L.; Dai, S.; Lopez-Zepeda, K.; Pham, N.; Graham, G. W.; Pan, X.; Christopher, P., Catalyst Architecture for Stable Single Atom Dispersion Enables Site-Specific Spectroscopic and Reactivity Measurements of Co Adsorbed to Pt Atoms, Oxidized Pt Clusters, and Metallic Pt Clusters on Tio2. *Journal of the American Chemical Society* **2017**, *139*, 14150-14165.

7. Yan, H.; Cheng, H.; Yi, H.; Lin, Y.; Yao, T.; Wang, C.; Li, J.; Wei, S.; Lu, J., Single-Atom Pd1/Graphene Catalyst Achieved by Atomic Layer Deposition: Remarkable Performance in Selective Hydrogenation of 1,3-Butadiene. *Journal of the American Chemical Society* **2015**, *137*, 10484-10487.

8. Jones, J., et al., Thermally Stable Single-Atom Platinum-on-Ceria Catalysts Via Atom Trapping. *Science* **2016**, *353*, 150.

9. Zhu, C.; Fu, S.; Shi, Q.; Du, D.; Lin, Y., Single-Atom Electrocatalysts. *Angewandte Chemie International Edition* **2017**, *56*, 13944-13960.

10. Campbell, C. T., The Energetics of Supported Metal Nanoparticles: Relationships to Sintering Rates and Catalytic Activity. *Accounts of Chemical Research* **2013**, *46*, 1712-1719.

11. Zhang, B.; Asakura, H.; Zhang, J.; Zhang, J.; De, S.; Yan, N., Stabilizing a Platinum1 Single-Atom Catalyst on Supported Phosphomolybdic Acid without Compromising Hydrogenation Activity. *Angewandte Chemie International Edition* **2016**, *55*, 8319-8323.

12. Campbell, C. T.; Mao, Z., Chemical Potential of Metal Atoms in Supported Nanoparticles: Dependence Upon Particle Size and Support. *ACS Catalysis* **2017**, *7*, 8460-8466.

13. Taylor, M. G.; Austin, N.; Gounaris, C. E.; Mpourmpakis, G., Catalyst Design Based on Morphology- and Environment-Dependent Adsorption on Metal Nanoparticles. *ACS Catalysis* **2015**, *5*, 6296-6301.

14. Lin, J.; Wang, A.; Qiao, B.; Liu, X.; Yang, X.; Wang, X.; Liang, J.; Li, J.; Liu, J.; Zhang, T., Remarkable Performance of Ir1/Feox Single-Atom Catalyst in Water Gas Shift Reaction. *Journal of the American Chemical Society* **2013**, *135*, 15314-15317.

15. Campbell, C. T., Electronic Perturbations. *Nature Chemistry* **2012**, *4*, 597.

16. Qiao, B.; Liang, J.-X.; Wang, A.; Xu, C.-Q.; Li, J.; Zhang, T.; Liu, J. J., Ultrastable Single-Atom Gold Catalysts with Strong Covalent Metal-Support Interaction (Cmsi). *Nano Research* **2015**, *8*, 2913-2924.

17. Zhang, Z., et al., Thermally Stable Single Atom Pt/M-Al2o3 for Selective Hydrogenation and Co Oxidation. *Nature Communications* **2017**, *8*, 16100.

18. Liu, J., Advanced Electron Microscopy of Metal–Support Interactions in Supported Metal Catalysts. *ChemCatChem* **2011**, *3*, 934-948.

19. O'Connor, N. J.; Jonayat, A. S. M.; Janik, M. J.; Senftle, T. P., Interaction Trends between Single Metal Atoms and Oxide Supports Identified with Density Functional Theory and Statistical Learning. *Nature Catalysis* **2018**, *1*, 531-539.

20. Campbell, C. T.; Sellers, J. R. V., Anchored Metal Nanoparticles: Effects of Support and Size on Their Energy, Sintering Resistance and Reactivity. *Faraday Discussions* **2013**, *162*, 9-30.

21. Nørskov, J. K.; Bligaard, T.; Rossmeisl, J.; Christensen, C. H., Towards the Computational Design of Solid Catalysts. *Nature Chemistry* **2009**, *1*, 37.

22. Noronha, F. B.; Fendley, E. C.; Soares, R. R.; Alvarez, W. E.; Resasco, D. E., Correlation between Catalytic Activity and Support Reducibility in the Co2 Reforming of Methane over Pt/Cexzr1−Xo2 Catalysts. *Chemical Engineering Journal* **2001**, *82*, 21-31.

23. Cui, X.; Li, W.; Ryabchuk, P.; Junge, K.; Beller, M., Bridging Homogeneous and Heterogeneous Catalysis by Heterogeneous Single-Metal-Site Catalysts. *Nature Catalysis* **2018**, *1*, 385-397.

24. Zhang, H.; Liu, G.; Shi, L.; Ye, J., Single-Atom Catalysts: Emerging Multifunctional Materials in Heterogeneous Catalysis. *Advanced Energy Materials* **2017**, *8*, 1701343.

25. Ghosh, T. K.; Nair, N. N., Rh1/Γ-Al2o3 Single-Atom Catalysis of O2 Activation and Co Oxidation: Mechanism, Effects of Hydration, Oxidation State, and Cluster Size. *ChemCatChem* **2013**, *5*, 1811-1821.

26. Hu, P.; Huang, Z.; Amghouz, Z.; Makkee, M.; Xu, F.; Kapteijn, F.; Dikhtiarenko, A.; Chen, Y.; Gu, X.; Tang, X., Electronic Metal–Support Interactions in Single-Atom Catalysts. *Angewandte Chemie International Edition* **2014**, *53*, 3418-3421.

27. Yang, M.; Allard, L. F.; Flytzani-Stephanopoulos, M., Atomically Dispersed Au–(Oh)X Species Bound on Titania Catalyze the Low-Temperature Water-Gas Shift Reaction. *Journal of the American Chemical Society* **2013**, *135*, 3768-3771.

28. Qiao, B.; Wang, A.; Yang, X.; Allard, L. F.; Jiang, Z.; Cui, Y.; Liu, J.; Li, J.; Zhang, T., Single-Atom Catalysis of Co Oxidation Using Pt1/Feox. *Nature Chemistry* **2011**, *3*, 634.

29. Wang, L., et al., Atomic-Level Insights in Optimizing Reaction Paths for Hydroformylation Reaction over Rh/Coo Single-Atom Catalyst. *Nature Communications* **2016**, *7*, 14036.

30. Cui, X.; Junge, K.; Dai, X.; Kreyenschulte, C.; Pohl, M.-M.; Wohlrab, S.; Shi, F.; Brückner, A.; Beller, M., Synthesis of Single Atom Based Heterogeneous Platinum Catalysts: High Selectivity and Activity for Hydrosilylation Reactions. *ACS Central Science* **2017**, *3*, 580-585.

31. Wang, J.; Zhao, X.; Lei, N.; Li, L.; Zhang, L.; Xu, S.; Miao, S.; Pan, X.; Wang, A.; Zhang, T., Hydrogenolysis of Glycerol to 1,3-Propanediol under Low Hydrogen Pressure over Wox-Supported Single/Pseudo-Single Atom Pt Catalyst. *ChemSusChem* **2016**, *9*, 784-790.

32. Guo, X., et al., Direct, Nonoxidative Conversion of Methane to Ethylene, Aromatics, and Hydrogen. *Science* **2014**, *344*, 616.

33. Duarte, R. B.; Krumeich, F.; van Bokhoven, J. A., Structure, Activity, and Stability of Atomically Dispersed Rh in Methane Steam Reforming. *ACS Catalysis* **2014**, *4*, 1279-1286.

34. Moses-DeBusk, M.; Yoon, M.; Allard, L. F.; Mullins, D. R.; Wu, Z.; Yang, X.; Veith, G.; Stocks, G. M.; Narula, C. K., Co Oxidation on Supported Single Pt Atoms: Experimental and Ab Initio Density Functional Studies of Co Interaction with Pt Atom on Θ-Al2o3(010) Surface. *Journal of the American Chemical Society* **2013**, *135*, 12634-12645.

35. Gu, X.-K.; Qiao, B.; Huang, C.-Q.; Ding, W.-C.; Sun, K.; Zhan, E.; Zhang, T.; Liu, J.; Li, W.-X., Supported Single Pt1/Au1 Atoms for Methanol Steam Reforming. *ACS Catalysis* **2014**, *4*, 3886-3890.

36. Abbet, S.; Sanchez, A.; Heiz, U.; Schneider, W. D.; Ferrari, A. M.; Pacchioni, G.; Rösch, N., Acetylene Cyclotrimerization on Supported Size-Selected Pdn Clusters ($1 \leq N \leq 30$): One Atom Is Enough! *Journal of the American Chemical Society* **2000**, *122*, 3453-3457.

37. Sun, S., et al., Single-Atom Catalysis Using Pt/Graphene Achieved through Atomic Layer Deposition. *Scientific Reports* **2013**, *3*, 1775.

38. Lang, R., et al., Hydroformylation of Olefins by a Rhodium Single-Atom Catalyst with Activity Comparable to Rhcl(Pph3)3. *Angewandte Chemie International Edition* **2016**, *55*, 16054-16058.

39. Schrödinger, E., An Undulatory Theory of the Mechanics of Atoms and Molecules. *Physical Review* **1926**, *28*, 1049-1070.

40. Kohn, W., Nobel Lecture: Electronic Structure of Matter---Wave Functions and Density Functionals. *Reviews of Modern Physics* **1999**, *71*, 1253-1266.

41. Jones, R. O., Density Functional Theory: Its Origins, Rise to Prominence, and Future. *Reviews of Modern Physics* **2015**, *87*, 897-923.

42. Hohenberg, P.; Kohn, W., Inhomogeneous Electron Gas. *Physical Review* **1964**, *136*, B864-B871.

43. Kohn, W.; Sham, L. J., Self-Consistent Equations Including Exchange and Correlation Effects. *Physical Review* **1965**, *140*, A1133-A1138.

44. Perdew, J. P.; Chevary, J. A.; Vosko, S. H.; Jackson, K. A.; Pederson, M. R.; Singh, D. J.; Fiolhais, C., Atoms, Molecules, Solids, and Surfaces: Applications of the Generalized Gradient Approximation for Exchange and Correlation. *Physical Review B* **1992**, *46*, 6671-6687.

45. Ernzerhof, M.; Scuseria, G. E., Assessment of the Perdew–Burke–Ernzerhof Exchange-Correlation Functional. *The Journal of Chemical Physics* **1999**, *110*, 5029-5036.

46. Hutter, J.; Iannuzzi, M.; Schiffmann, F.; VandeVondele, J., Cp2k: Atomistic Simulations of Condensed Matter Systems. *Wiley Interdisciplinary Reviews: Computational Molecular Science* **2014**, *4*, 15-25.

47. Perdew, J. P.; Burke, K.; Ernzerhof, M., Generalized Gradient Approximation Made Simple. *Physical Review Letters* **1996**, *77*, 3865-3868.

48. Grimme, S.; Antony, J.; Ehrlich, S.; Krieg, H., A Consistent and Accurate Ab Initio Parametrization of Density Functional Dispersion Correction (Dft-D) for the 94 Elements H-Pu. *The Journal of Chemical Physics* **2010**, *132*, 154104.

49. Bengtsson, L., Dipole Correction for Surface Supercell Calculations. *Physical Review B* **1999**, *59*, 12301-12304.

50. VandeVondele, J.; Hutter, J., Gaussian Basis Sets for Accurate Calculations on Molecular Systems in Gas and Condensed Phases. *The Journal of Chemical Physics* **2007**, *127*, 114105.

51. Goedecker, S.; Teter, M.; Hutter, J., Separable Dual-Space Gaussian Pseudopotentials. *Physical Review B* **1996**, *54*, 1703-1710.

52. Hartwigsen, C.; Goedecker, S.; Hutter, J., Relativistic Separable Dual-Space Gaussian Pseudopotentials from H to Rn. *Physical Review B* **1998**, *58*, 3641-3662.

53. Krack, M., Pseudopotentials for H to Kr Optimized for Gradient-Corrected Exchange-Correlation Functionals. *Theoretical Chemistry Accounts* **2005**, *114*, 145-152.

54. Greenwood, N. N.; Earnshaw, A., *Chemistry of the Elements*, 2nd ed.; Butterworth-Heinemann: Oxford ; Boston, 1997, p xxii, 1341 p.

55. Lu, Q.; Ren, J.; Wang, Z., Using Genetic Programming with Prior Formula Knowledge to Solve Symbolic Regression Problem. *Computational intelligence and neuroscience* **2016**, *2016*, 1021378-1021378.

56. O'Reilly, U.-M., *Genetic Programming Theory and Practice Ii*; Springer: New York, 2005, p xiv, 320 p.

57. Koza, J. R.; Keane, M. A.; Streeter, M. J., What's Ai Done for Me Lately? Genetic Programming's Human-Competitive Results. *IEEE Intelligent Systems* **2003**, *18*, 25-31.

58. Schmidt, M.; Lipson, H., Distilling Free-Form Natural Laws from Experimental Data. *Science* **2009**, *324*, 81.

59. Tománek, D.; Mukherjee, S.; Bennemann, K. H., Simple Theory for the Electronic and Atomic Structure of Small Clusters. *Physical Review B* **1983**, *28*, 665-673.

60. Yan, Z.; Taylor, M. G.; Mascareno, A.; Mpourmpakis, G., Size-, Shape-, and Composition-Dependent Model for Metal Nanoparticle Stability Prediction. *Nano Letters* **2018**, *18*, 2696-2704.

61. Heiz, U.; Sanchez, A.; Abbet, S.; Schneider, W. D., Catalytic Oxidation of Carbon Monoxide on Monodispersed Platinum Clusters: Each Atom Counts. *Journal of the American Chemical Society* **1999**, *121*, 3214-3217.

62. Heiz, U.; Sanchez, A.; Abbet, S.; Schneider, W. D., Tuning the Oxidation of Carbon Monoxide Using Nanoassembled Model Catalysts. *Chemical Physics* **2000**, *262*, 189-200.

63. Hoffman, A. S.; Debefve, L. M.; Zhang, S.; Perez-Aguilar, J. E.; Conley, E. T.; Justl, K. R.; Arslan, I.; Dixon, D. A.; Gates, B. C., Beating Heterogeneity of Single-Site Catalysts: Mgo-Supported Iridium Complexes. *ACS Catalysis* **2018**, *8*, 3489-3498.

64. Stair, P. C., The Concept of Lewis Acids and Bases Applied to Surfaces. *Journal of the American Chemical Society* **1982**, *104*, 4044-4052.

65. Kostetskyy, P.; Nolan, C. M.; Dixit, M.; Mpourmpakis, G., Understanding Alkane Dehydrogenation through Alcohol Dehydration on Γ-Al2o3. *Industrial & Engineering Chemistry Research* **2018**, *57*, 16657-16663.

66. Díez, V. K.; Apesteguía, C. R.; Di Cosimo, J. I., Acid–Base Properties and Active Site Requirements for Elimination Reactions on Alkali-Promoted Mgo Catalysts. *Catalysis Today* **2000**, *63*, 53-62.

67. Evans, O. R.; Bell, A. T.; Tilley, T. D., Oxidative Dehydrogenation of Propane over Vanadia-Based Catalysts Supported on High-Surface-Area Mesoporous Mgal2o4. *Journal of Catalysis* **2004**, *226*, 292-300.

68. Lou, Y.; Liu, J., Co Oxidation on Metal Oxide Supported Single Pt Atoms: The Role of the Support. *Industrial & Engineering Chemistry Research* **2017**, *56*, 6916-6925.

69. Van't Blik, H. F. J.; Van Zon, J. B. A. D.; Huizinga, T.; Vis, J. C.; Koningsberger, D. C.; Prins, R., Structure of Rhodium in an Ultradispersed Rhodium/Alumina Catalyst as Studied by Exafs and Other Techniques. *Journal of the American Chemical Society* **1985**, *107*, 3139-3147.

70. Sanchez, A.; Abbet, S.; Heiz, U.; Schneider, W. D.; Häkkinen, H.; Barnett, R. N.; Landman, U., When Gold Is Not Noble: Nanoscale Gold Catalysts. *The Journal of Physical Chemistry A* **1999**, *103*, 9573-9578.

71. Lu, Y., et al., Identification of the Active Complex for Co Oxidation over Single-Atom Ir-on-Mgal2o4 Catalysts. *Nature Catalysis* **2019**, *2*, 149-156.

72. Pacchioni, G., Electronic Interactions and Charge Transfers of Metal Atoms and Clusters on Oxide Surfaces. *Physical Chemistry Chemical Physics* **2013**, *15*, 1737-1757.

73. Kittel, C., *Introduction to Solid State Physics*, 8th ed.; Wiley: Hoboken, NJ, 2005, p xix, 680 p.

74. Haynes, W. M., *Crc Handbook of Chemistry and Physics, 92nd Edition*; CRC Press: Hoboken, 2011.

75. Hu, S.-Z.; Zhou, Z.-H.; Robertson, B. E., Consistent Approaches to Van Der Waals Radii for the Metallic Elements. In *Zeitschrift für Kristallographie International journal for structural, physical, and chemical aspects of crystalline materials*, 2009; Vol. 224, p 375.

76. Mantina, M.; Chamberlin, A. C.; Valero, R.; Cramer, C. J.; Truhlar, D. G., Consistent Van Der Waals Radii for the Whole Main Group. *The Journal of Physical Chemistry A* **2009**, *113*, 5806-5812.

77. Pyykkö, P.; Riedel, S.; Patzschke, M., Triple-Bond Covalent Radii. *Chemistry – A European Journal* **2005**, *11*, 3511-3520.

78. Zhang, Y.; Evans, J. R. G.; Yang, S., Corrected Values for Boiling Points and Enthalpies of Vaporization of Elements in Handbooks. *Journal of Chemical & Engineering Data* **2011**, *56*, 328-337.

79. Nelder, J. A.; Mead, R., A Simplex Method for Function Minimization. *The Computer Journal* **1965**, *7*, 308-313.

80. Shannon, R., Revised Effective Ionic Radii and Systematic Studies of Interatomic Distances in Halides and Chalcogenides. *Acta Crystallographica Section A* **1976**, *32*, 751-767.